AIAA JOURNAL
Vol. 37, No. 5, May 1999

Monotonically Integrated Large Eddy Simulation of Free Shear Flows

C. Fureby*
FOA Defence Research Establishment, S-172 90 Stockholm, Sweden
and
F. F. Grinstein†
U.S. Naval Research Laboratory, Washington, D.C. 20375-5344

With a view to ensure that proper interaction between resolvable or grid scale and subgrid scale (SGS) motions are mimicked, it is vital to determine the necessary physics that must be built into the SGS models. In ordinary large eddy simulation (LES) approaches, models are introduced for closure in the low-pass filtered Navier–Stokes equations (NSEs), which are the ones solved numerically. A promising LES approach is monotonically integrated LES (MILES), which involves solving the unfiltered NSE using high-resolution monotone algorithms; in this approach, implicit SGS models, provided by intrinsic nonlinear high-frequency filters built into the convection discretization, are coupled naturally to the resolvable scales of the flow. Formal properties of the effectual SGS modeling using MILES are documented using databases of simulated homogeneous turbulence and transitional freejets; mathematical and physical aspects of (implicit) SGS modeling through the use of nonlinear flux limiters are addressed in this context. Comparison of MILES and other conventional LES models applied to free shear flows are presented to confirm that the concept of LES is virtually independent of the SGS model if the resolution is fine enough to ensure that the cutoff wave number lies in the inertial subrange, provided that the LES model can adequately channel kinetic energy out of the resolved scales near the cutoff wave number, to prevent spurious energy buildup and aliasing.

Introduction

IMPORTANT issues that need to be addressed in numerical simulations of free shear flows in the high-Reynolds-numberregime relate to the appropriate modeling of the required boundary conditions for flows developing in space and time in finite-size computationaldomain simulations, i.e., supergrid modeling,[1] and the unresolved subgrid flow features. Thus, subgrid scale (SGS) models are required to attest the proper evolution of three-dimensionaltime-dependent details of the resolvable or grid scale (GS) part of the motion responsible for the primary transport and entrainment. At high Reynolds numbers of practical interest, direct numerical simulation (DNS) may not be used to resolve all scales of motion, so that SGS turbulence modeling becomes unavoidable, while resolving accurately the large scale flow governing the evolution of coherent flow structures. In the traditional large eddy simulation (LES) approach, cf. Ref. 2, SGS models are explicitly introduced in the low-pass filtered Navier–Stokes equations (NSEs); these include SGS closures developed in physical space, such as algebraic, one-equation eddy-viscosity, scale similarity, and differential stress models, of which the former can be both of nondynamic[3] and dynamic nature,[4] and SGS models developed in some adjoint space, such as the renormalization group[5] (RNG) or the eddy-damped quasinormal Markovian[6] (EDQNM) models.

Mathematical and physical constraints of LES implementation have been the subject of recent studies including LES equations and commutation errors,[7] the role of discretization errors,[8] and the concepts of frame indifference[9] and realizability.[10] For isothermal low-Mach-numberflows, the resolved structures appear to be largely unaffected by the specifics of the SGS models, e.g., Refs. 11 and 12. In other flows, the unresolved small-scale physics may be of importance in driving the development and maintenance of the three-dimensional features. Therefore, it is important to determine the minimal physics that must be included in the SGS models to ensure that the proper interactions between GSs and SGSs are appropriately emulated.

In conventional LES explicit SGS models are introduced for closure and to provide a mechanism by which dissipation of kinetic energy accumulated at high wave numbers can occur. A promising alternative for high-Reynolds-number flows involves solving the NSE with high-resolution monotone algorithms, such as the flux-corrected transport (FCT) method or the piecewise parabolic method (PPM) without explicitly using SGS models, which has been denoted monotonically integrated LES[13] (MILES); with these methods, nonlinear high-frequency filters built into the algorithms provide implicit SGS models, and, thus, explicit SGS models can be dispensed with. Examples of successful applications of nonmonotone, implicitly implemented SGS models have also been reported, e.g., Ref. 14. For high-Reynolds-numberfree shear flows, a rationale supporting the use of MILES can be given based on the essentially inviscid features of the vorticity dynamics, which at the smallest scale is characterized by elongated tubelike (worm) vortices, typically much thinner than the main flow scales[12,15,16]; this suggests that nearly inviscid methods capable of handling vortices in a manner similar to that of shock-capturing schemes might provide an efficient computational framework in such flow regimes. Similar ideas have been also envisaged as the premise of the contour dynamics,[17] for example, and the vorticity confinement methods, e.g., Ref. 18.

Applications of MILES using PPM have included studies of decaying supersonic homogeneous turbulent flow[16] and supersonic confined mixing layers.[19] Recent applications of MILES using FCT to freejets have included axisymmetric[20] and rectangular[21,22] configurations at moderately high Reynolds number. Convergence studies and turbulence decay investigations[16] indicate that MILES is capable of capturing the dominant inertial subrange of the energy spectrum with a self-similar simulated dissipation range. Comparative studies with MILES and other LES models of nonreactive[9] and reactive shear flows[23] suggest that LES results are fairly resilient to the SGS modeling provided that the cutoff wavelength is within the inertial subrange. Moreover, turbulent shear flow MILES studies based on the Euler equations, e.g., Refs. 12 and 16, suggest that

Presented as Paper 98-0537 at the AIAA 36th Aerospace Sciences Meeting, Reno, NV, Jan. 12–15, 1998; received April 13, 1998; revision received Jan. 5, 1999; accepted for publication Jan. 11, 1999.

*Senior Researcher, Department of Weapons and Protection, Division of Warheads and Propulsion. Member AIAA.

†Research Physicist, Laboratory for Computational Physics and Fluid Dynamics Code 6410. Associate Fellow AIAA.

some features of the inertial subrange might be independent of the exact nature of turbulent dissipation, giving further indication of the resiliency of high-Reynolds-number free shear flow to the intrinsic details of the SGS modeling. These results encourage the use of MILES in the study of high-Reynolds-number free shear flows and motivate our investigation of the formal properties of the approach including comparisons with other more conventional LES schemes.

Governing Equations and the Conventional LES Model

The fluid dynamic model used in the following study is based on the nonhomogeneous compressible NSE.[24] The working hypothesis in conventional LES is the postulate that all dependent variables can be divided into GS and SGS components, i.e., $\Phi = \bar{\Phi} + \Phi'$. The resolvable GS components are defined as $\bar{\Phi} = G * \Phi$, where the kernel $G = G(\boldsymbol{x}, \Delta)$ is any function of $\boldsymbol{x}$ and the width $\Delta = \Delta(\boldsymbol{x})$ endowed with the properties

$$\int G(\boldsymbol{x}, \Delta)\, \mathrm{d}^3x = 1, \qquad \lim_{\Delta \to 0} G(\Delta, \boldsymbol{x}) = \delta(\boldsymbol{x})$$

$$G(\boldsymbol{x}, \Delta) \in C^n(\mathbb{R}^3)$$

having compact support in the computational domain D having the boundary ∂D and closure $D \cup \partial D$. The LES equations are obtained by convolving the NSE with G, noticing that

$$[\nabla, G*]\Phi = \left(\frac{\partial G}{\partial \Delta} * \Phi\right) \mathrm{grad}\, \Delta + (G\Phi \boldsymbol{n})_{\partial D}$$

$$[\partial_t, G*]\Phi = 0$$

where $\boldsymbol{n}$ is the outward pointing unit normal to ∂D (Ref. 25). Following Refs. 7 and 25, it is evident that this lack of commutation produces additional terms in the LES equations. An order of magnitude analysis (using Taylor series expansions in $\partial^k G/\partial \Delta^k$) shows that these error terms are of $\mathcal{O}(\Delta^2)$, whereas the SGS models, div $\boldsymbol{B}$ and div $\boldsymbol{b}$, are of $\mathcal{O}(\Delta^{n-1})$ because $\boldsymbol{B}$ and $\boldsymbol{b}$ are of $\mathcal{O}(\Delta^n)$, where $\frac{4}{3} < n < 2$. The conventional LES equations, thus, follow as a first-order approximation,

$$\partial_t(\bar{\rho}) + \mathrm{div}(\bar{\rho}\tilde{\boldsymbol{v}}) = 0 \tag{1a}$$

$$\partial_t(\bar{\rho}\tilde{\boldsymbol{v}}) + \mathrm{div}(\bar{\rho}\tilde{\boldsymbol{v}} \otimes \tilde{\boldsymbol{v}}) = -\mathrm{grad}\, \bar{p} + \mathrm{div}(\bar{\boldsymbol{S}} - \boldsymbol{B}) + \bar{\rho}\tilde{\boldsymbol{g}} \tag{1b}$$

$$\partial_t(\bar{\rho}\tilde{e}) + \mathrm{div}(\bar{\rho}\tilde{\boldsymbol{v}}\tilde{e}) = \mathrm{div}(\bar{\boldsymbol{h}} - \boldsymbol{b}) - \bar{p}\, \mathrm{div}\, \tilde{\boldsymbol{v}} + \bar{\boldsymbol{S}} \cdot \tilde{\boldsymbol{D}} + \pi + \varepsilon + \bar{\rho}\tilde{\sigma} \tag{1c}$$

where the tilde denotes Favré averaging, ρ is the density, $\boldsymbol{v}$ is the velocity, p is the pressure, and $\boldsymbol{S} = \eta\, \mathrm{tr}\boldsymbol{D}\boldsymbol{I} + 2\mu \boldsymbol{D}_D$, where $\mu = \rho\nu$ is the molecular viscosity, η is the bulk viscosity, and $\boldsymbol{D}_D = \boldsymbol{D} - \frac{1}{3}\mathrm{tr}\boldsymbol{D}\boldsymbol{I}$ and $\boldsymbol{D} = \frac{1}{2}(\mathrm{grad}\, \boldsymbol{v} + \mathrm{grad}\, \boldsymbol{v}^T)$. $\boldsymbol{B} = \bar{\rho}(\widetilde{\boldsymbol{v} \otimes \boldsymbol{v}} - \tilde{\boldsymbol{v}} \otimes \tilde{\boldsymbol{v}})$ is the SGS stress tensor, $\boldsymbol{g}$ is the specific body force, e is the specific internal energy, and $\boldsymbol{h} = \kappa\, \mathrm{grad}\, e$, where κ is the thermal conductivity. $\boldsymbol{b} = \bar{\rho}(\widetilde{e\boldsymbol{v}} - \tilde{e}\tilde{\boldsymbol{v}})$ is the SGS flux vector, $\pi = \overline{p\, \mathrm{div}\, \boldsymbol{v}} - \bar{p}\, \mathrm{div}\, \tilde{\boldsymbol{v}}$ is the SGS pressure dilatation, $\varepsilon = \overline{\boldsymbol{S} \cdot \boldsymbol{D}} - \bar{\boldsymbol{S}} \cdot \tilde{\boldsymbol{D}}$ is the SGS dissipation, and σ is the nonmechanical net power.

Models for $\boldsymbol{B}, \boldsymbol{b}, \pi$, and ε are required to complete the LES equations and to provide for the interaction between the large- and small-scale components. Following Ref. 26, $\boldsymbol{B}$ and $\boldsymbol{b}$ can be decomposed into the following: Leonard terms $\boldsymbol{L}$ and $\boldsymbol{I}$, which are interactions of resolved eddies to generate small-scale turbulence; cross terms $\boldsymbol{C}$ and $\boldsymbol{c}$, which are interactions between resolved and unresolved eddies and, thus, energy transfer in either direction, although mainly toward the small-scale eddies; and Reynolds terms $\boldsymbol{R}$ and $\boldsymbol{r}$, which are interactions between small-scale eddies producing most of the energy transfer from the large to the small scales. From mathematical analysis and physical considerations,[7,8,10,25,27] $\boldsymbol{B}$ (and $\boldsymbol{b}$) are known to be Grammian tensors provided that $G = G(|\boldsymbol{x}|, \Delta)$, i.e., $G \in SU(3)$, also implying that $\boldsymbol{B} \in P\mathrm{sym}$, where $P\mathrm{sym}$ is the set of all positive symmetric definite tensors. Moreover, because $\boldsymbol{B}$ and $\boldsymbol{b}$ are frame indifferent,[25] they are also isotropic functions of their arguments. The realizability conditions follows from the Grammian nature of $\boldsymbol{B}$, and the necessary and sufficient conditions for $\boldsymbol{B} \in P\mathrm{sym}$ can be expressed using the principal invariants of $\boldsymbol{B}$, i.e., $\frac{1}{2}\,\mathrm{tr}\boldsymbol{B} \geq 0$, $\frac{1}{2}[(\mathrm{tr}\boldsymbol{B})^2 - \mathrm{tr}(\boldsymbol{B}^2)] \geq 0$, and $\det \boldsymbol{B} \geq 0$.

The most popular closure models for $\boldsymbol{B}$ and $\boldsymbol{b}$ are based on gradient hypotheses in which the SGS models assume bijective correlations: $\boldsymbol{B} = \frac{2}{3}(\bar{\rho}k - \mu_k\, \mathrm{div}\, \tilde{\boldsymbol{v}})\boldsymbol{I} - 2\mu_k \tilde{\boldsymbol{D}}_D$ and $\boldsymbol{b} = -2\kappa_k\, \mathrm{grad}\, \tilde{e}$, where k, μ_k, and κ_k are the SGS kinetic energy, eddy viscosity, and diffusivity, respectively, which have to be separately modeled. When the turbulence is three dimensional, the Smagorinsky model (SMG) is often used in which $\mu_k = c_D \bar{\rho} \Delta^2 \|\tilde{\boldsymbol{D}}\|$ and $\kappa_k = \mu_k/Pr$, where Pr is the turbulent Prandtl number.[3] Alternatively, in the one-equation eddy-viscosity model (OEEVM) k is obtained directly from a modeled balance equation,[28] whereas $\mu_k = c_k \bar{\rho} \Delta \sqrt{k}$ and $\kappa_k = \mu_k/Pr_T$. The model coefficients can be determined from the assumption of isotropy and a $|\boldsymbol{k}|^{-5/3}$ inertial subrange behavior, but this approach is questionable in transient situations or in the proximity of wall boundaries. This provides the motivation for dynamic eddy-viscosity models, where an attempt is made to evaluate the model coefficients dynamically through a second level of filtering.[4] The model coefficients can also be evaluated using methods based on RNG[5] or EDQNM.[6] Because of the poor correlation between the exact SGS stress tensor and the eddy-viscosity models (as evaluated from DNS data),[26] scale-similarity models[29] with $\boldsymbol{B} = \bar{\rho}(\tilde{\tilde{\boldsymbol{v}}} \otimes \tilde{\tilde{\boldsymbol{v}}} - \tilde{\boldsymbol{v}} \otimes \tilde{\boldsymbol{v}})$ and $\boldsymbol{b} = \bar{\rho}(\tilde{\tilde{\boldsymbol{v}}}\tilde{\tilde{e}} - \tilde{\tilde{\boldsymbol{v}}}\tilde{e})$ were suggested. To incorporate SGS diffusion, this model has been combined with eddy-viscosity models to give the mixed model of Erlebacher et al.[29] In general, the SGS models satisfy the realizability constraints [the exception is $\det \boldsymbol{B} \geq 0$ (Ref. 25)] if the model coefficients are chosen with care. Models for π are not extensively elaborated on,[29] although much attention has been paid to ε (Ref. 30).

The LES equations and the SGS model of choice are here discretized using an unstructured finite volume method so that $D \cup \partial D \to T_\Delta$, where T_Δ is a partition of $D \cup \partial D$ into subvolumes Ω_P, of the characteristic size Δ, having centroids at $\boldsymbol{x}_P$ and face-area centroids at $\boldsymbol{x}_f$, satisfying the conditions $\cup_P(\Omega_P) = D \cup \partial D$ and $\cap_P(\Omega_P) = \emptyset$. Letting

$$\Phi_P = \frac{1}{\delta V} \int_{\Omega_P} \Phi\, \mathrm{d}V$$

represent the discrete approximation to the cell average of Φ over the Pth cell, Gauss theorem can be used to obtain the semidiscretized LES equations. These are integrated in time by multistep methods[31] to give the fully discretized LES equations; more precisely this may be expressed according to

$$\sum_{i=1}^{m} \left[\alpha_i \bar{\rho}_P^{n+i} + \frac{\beta_i \Delta t}{\mathrm{d}V_P} \sum_f (\bar{\rho}\tilde{\boldsymbol{v}} \cdot \mathrm{d}\boldsymbol{A})_f^{n+i} \right] = 0 \tag{2a}$$

$$\sum_{i=1}^{m} \left\{ \alpha_i (\bar{\rho}\tilde{\boldsymbol{v}})_P^{n+i} + \frac{\beta_i \Delta t}{\mathrm{d}V_P} \sum_f [(\bar{\rho}\tilde{\boldsymbol{v}} \cdot \mathrm{d}\boldsymbol{A})\tilde{\boldsymbol{v}} - (\bar{\boldsymbol{S}} - \boldsymbol{B})\, \mathrm{d}\boldsymbol{A}]_f^{n+i} + \beta_i (\bar{\rho}\tilde{\boldsymbol{g}})_p^{n+i} \Delta t \right\} = -\beta_i (\mathrm{grad}\, \bar{p})_p^{n+i} \Delta t \tag{2b}$$

$$\sum_{i=1}^{m} \left\{ \alpha_i (\bar{\rho}\tilde{e})_P^{n+i} + \frac{\beta_i \Delta t}{\mathrm{d}V_P} \sum_f [(\bar{\rho}\tilde{\boldsymbol{v}} \cdot \mathrm{d}\boldsymbol{A})\tilde{e} - (\bar{\boldsymbol{h}} - \boldsymbol{b}) \cdot \mathrm{d}\boldsymbol{A}]_f^{n+i} - \beta_i (\bar{p}\, \mathrm{div}\, \tilde{\boldsymbol{v}} + \bar{\boldsymbol{S}} \cdot \tilde{\boldsymbol{D}} + \pi + \varepsilon + \bar{\rho}\tilde{\sigma})_P \Delta t \right\} = 0 \tag{2c}$$

where α_i and β_i are parameters of the scheme, Δt is the time step, $\mathrm{d}V_P$ is the volume of Ω_P, and $\mathrm{d}\boldsymbol{A}_f$ is the face-area vector of face f of Ω_P satisfying $\cup_f(|\mathrm{d}\boldsymbol{A}_f|) = \partial\Omega_P$ and $\cap_f(|\mathrm{d}\boldsymbol{A}_f|) = \emptyset$. Let the convective flux functions $\tilde{\boldsymbol{f}}_f^C(\tilde{\boldsymbol{v}}; \mu)$ and $\tilde{f}_f^C(\tilde{e}; \mu)$ represent approximations to the convective fluxes $\boldsymbol{f}_f^C(\tilde{\boldsymbol{v}}) = ((\tilde{\boldsymbol{v}} \cdot \mathrm{d}\boldsymbol{A})\tilde{\boldsymbol{v}})_f$ and $f_f^C(\tilde{e}) = ((\tilde{\boldsymbol{v}} \cdot \mathrm{d}\boldsymbol{A})\tilde{e})_f$, respectively, and the combined flux functions $\tilde{\boldsymbol{f}}_f^D(\tilde{\boldsymbol{v}}; \mu)$ and $\tilde{f}_f^D(\tilde{e}; \mu)$ represent approximations to the mixed diffusive and SGS fluxes $\boldsymbol{f}_f^D(\tilde{\boldsymbol{v}}) = ((\bar{\boldsymbol{S}} - \boldsymbol{B})\mathrm{d}\boldsymbol{A})_f$ and $f_f^D(\tilde{e}) = ((\bar{\boldsymbol{h}} - \boldsymbol{b}) \cdot \mathrm{d}\boldsymbol{A})_f$. Here, $\mu = \mu(P)$ represents a set of grid points in a neighborhood of P. The functional dependencies of the convective and combined fluxes on the nodal values of the dependent variables, often referred

to as the functional reconstruction, defines the method. Because the SGS contributions to the conventional LES equations are of $\mathcal{O}(\Delta^{n-1})$ and $\Delta = \mathcal{O}(|\boldsymbol{d}|)$, where $|\boldsymbol{d}|$ is the characteristic grid spacing, the leading-order truncation error of the modified LES equations are required to be of $\mathcal{O}(|\boldsymbol{d}|^{(n-1)+1})$ or the SGS models will be impaired. Hence, the spatial discretization should be of second-order accuracy or higher. For a given accuracy, several possibilities exist for the flux functions $\tilde{\boldsymbol{f}}_f^C(\tilde{\boldsymbol{v}};\mu)$, $\tilde{f}_f^C(\tilde{e};\mu)$, $\tilde{\boldsymbol{f}}_f^D(\tilde{\boldsymbol{v}};\mu)$, and $\tilde{f}_f^D(\tilde{e};\mu)$. For instance, if a first-order functional reconstruction is used for the convective fluxes, i.e., $\tilde{\boldsymbol{f}}_f^C = \tilde{\boldsymbol{f}}_f^C(\tilde{\boldsymbol{v}};P,N)$ and $\tilde{f}_f^C = \tilde{f}_f^C(\tilde{e};P,N)$, where N represents the neighbors of P, central difference methods of second-order accuracy are recovered. Also, if the inner gradients to $\tilde{\boldsymbol{f}}_f^D(\tilde{\boldsymbol{v}};\mu)$ and $\tilde{f}_f^D(\tilde{e};\mu)$ are approximated by central differencing, i.e., $\tilde{\boldsymbol{f}}_f^D = \tilde{\boldsymbol{f}}_f^D(\tilde{\boldsymbol{v}};P,N)$ and $\tilde{f}_f^D = \tilde{f}_f^D(\tilde{e};P,N)$, then second-order central difference approximations also result for the combined fluxes. For consistency reasons, the time integration should be carried out using a second-order accurate method such as Crank–Nicholson. The resulting discretized equations can then be solved using different techniques depending on other aspects of the fluid dynamic problem to be investigated.

MILES Model

In constructing a mental picture supporting MILES, we recognize that slender, tubelike vortices, observed in DNS and LES studies, e.g., Refs. 12, 15, and 16, characterize the vorticity dynamics of high-Reynolds-number free shear flow at the smallest scale; when these worm vortices are much thinner than the main flow scales, we expect that details of the internal vortex structure will not be significant and that the dominant dynamical features will involve only the strengths and positions of their centerlines. In addition, we note that for high-Reynolds-number important vortex interaction mechanisms, such as vortex merger and reconnection, occur on convective timescales shorter than the diffusive timescales and are, thus, essentially inviscid. However, a minimal nominal diffusion is required to trigger vortex merger or reconnection processes, which cannot occur in an inviscid fluid. For such flows, we conjecture that methods that will handle vortices in a manner similar to shocks will provide an efficient computational framework.

The traditional approach in Eulerian shock capturing methods, which attempt to represent the movement of a shock or a discontinuity, usually being much thinner than one cell, is to introduce artificial viscosity to damp spurious oscillations in regions of sharp gradients, thereby spreading the discontinuity over distances that can be resolved on the grid, as overshoots and undershoots are damped. Because artificial viscosity is typically needed only near discontinuities, it should depend directly on the evolving solution, being larger near discontinuities than in smooth regions. Furthermore, the artificial viscosity is required to vanish as $\Delta \to 0$ and $\Delta t \to 0$, so that it remains consistent with the partially hyperbolic nature of the NSE. From a numerical point of view, the SGS viscosity in eddy-viscosity-type models has similar properties and effects.

Because the main goal of LES is to accurately simulate the behavior of the three-dimensional time-dependent details of the large-scale energy containing eddies, high-resolution methods are required. The term high resolution applies here to methods that are at least second-order accurate on smooth solutions and yet give well-resolved, nonoscillatory solutions in the vicinity of steep gradients. However, according to Godunov,[32] there are no linear second-order or higher-order methods that guarantee monotonicity, and therefore nonlinear monotone-preserving methods must be used. The fundamental feature of such methods is that they use nonlinear flux limiting or flux correcting in an attempt to maintain high resolution at the same time that monotonicity is guaranteed.

In MILES, the NSE can be discretized using the same unstructured finite volume method as used for the LES Eqs. (1), and these are integrated in time by the same multistep method:

$$\sum_{i=1}^{m}\left[\alpha_i \rho_P^{n+i} + \frac{\beta_i \Delta t}{\mathrm{d}V_P}\sum_f (\rho \boldsymbol{v}\cdot \mathrm{d}\boldsymbol{A})_f^{n+i}\right] = 0 \tag{3a}$$

$$\sum_{i=1}^{m}\left\{\alpha_i (\rho \boldsymbol{v})_P^{n+i} + \frac{\beta_i \Delta t}{\mathrm{d}V_P}\sum_f [(\rho \boldsymbol{v}\cdot \mathrm{d}\boldsymbol{A})\boldsymbol{v} - \boldsymbol{S}\,\mathrm{d}\boldsymbol{A}]_f^{n+i} + \beta_i (\rho \boldsymbol{g})_p^{n+i}\Delta t\right\} = -\beta_i (\mathrm{grad}\, p)_p^{n+i}\Delta t \tag{3b}$$

$$\sum_{i=1}^{m}\left\{\alpha_i (\rho e)_P^{n+i} + \frac{\beta_i \Delta t}{\mathrm{d}V_P}\sum_f [(\rho \boldsymbol{v}\cdot \mathrm{d}\boldsymbol{A})e - \boldsymbol{h}\cdot \mathrm{d}\boldsymbol{A}]_f^{n+i} - \beta_i (p\,\mathrm{div}\,\boldsymbol{v} + \boldsymbol{S}\cdot\boldsymbol{D} + \rho\sigma)_P \Delta t\right\} = 0 \tag{3c}$$

Similarly, the convective flux functions $\tilde{\boldsymbol{f}}_f^C(\boldsymbol{v};\mu)$ and $\tilde{f}_f^C(e;\mu)$ represent approximations to the convective fluxes $\boldsymbol{f}_f^C(\boldsymbol{v}) = [(\boldsymbol{v}\cdot \mathrm{d}\boldsymbol{A})\boldsymbol{v}]_f$ and $f_f^C(e) = [(\boldsymbol{v}\cdot \mathrm{d}\boldsymbol{A})e]_f$, and the flux functions $\tilde{\boldsymbol{f}}_f^D(\boldsymbol{v};\mu)$ and $\tilde{f}_f^D(e;\mu)$ represent approximations to the viscous and diffusive fluxes $\boldsymbol{f}_f^D(\boldsymbol{v}) = (\boldsymbol{S}\mathrm{d}\boldsymbol{A})_f$ and $f_f^D(e) = (\boldsymbol{h}\cdot \mathrm{d}\boldsymbol{A})_f$. A fundamental difference between conventional LES and MILES, apparent from comparing Eqs. (2) and (3), is that the nodal values of the dependent variables in the conventional LES model are obtained from successive filtering and cell averaging,

$$\bar{\Phi}_P = \frac{1}{\delta V_P}\int_{\Omega_P} (G * \Phi)\,\mathrm{d}V$$

whereas in MILES they are obtained from cell averaging only:

$$\Phi_P = \frac{1}{\delta V_P}\int_{\Omega_P} \Phi\,\mathrm{d}V$$

However, in practical LES implementation the prefiltering has no explicit effect on the variables that are solved for because this filtering operation is performed when deriving the LES equations, which are then to be discretized. The prefiltering has the indirect effect of producing unresolved transport or SGS terms that require additional closure modeling, thus affecting the equations to be solved and their solution. It may then be argued that the cell averaging is a builtin filtering procedure using essentially a top-hat kernel.

For flux-limiting methods, we choose a high-order convective flux function $\tilde{f}_f^H$ that works well in smooth regions and a low-order convective flux function $\tilde{f}_f^L$ (typically some unconditionally monotone method such as upwind differencing) that behaves well near discontinuities. We then attempt to hybridize these two into a single flux function in such a way that $\tilde{f}_f^C(\Phi;\mu)$ reduces to $\tilde{f}_f^H(\Phi;\mu)$ in smooth regions and to $\tilde{f}_f^L(\Phi;\mu)$ near discontinuities. Mathematically,

$$\tilde{f}_f^C(\Phi;\mu) = \tilde{f}_f^L(\Phi;\mu) + \Gamma(\Phi;\mu)\left[\tilde{f}_f^H(\Phi;\mu) - \tilde{f}_f^L(\Phi;\mu)\right] \tag{4}$$

where $\Gamma(\Phi;\mu)$ is the flux limiter. If the field Φ is smooth near Φ_P, then $\Gamma(\Phi;\mu)$ should be near unity, whereas in the vicinity of a discontinuity, we require $\Gamma(\Phi;\mu)$ to be near zero. Note that

$$\tilde{f}_f^C(\Phi;\mu) = \tilde{f}_f^H(\Phi;\mu) - [1-\Gamma(\Phi;\mu)]\left[\tilde{f}_f^H(\Phi;\mu) - \tilde{f}_f^L(\Phi;\mu)\right] \tag{5}$$

One of the earliest high-resolution methods, the FCT method[33] can be viewed as a flux-limiter method. The correction term $[\tilde{f}_f^H(\Phi;\mu) - \tilde{f}_f^L(\Phi;\mu)]$ is referred to as the antidiffusive flux because the low-order flux contains too much diffusion for smooth data and the correction compensates for this. The FCT strategy is to incorporate as much as possible of the antidiffusive flux without violating causality, positivity, and monotonicity.

Historically, monotonicity preserving methods are associated with the property that, if a dependent variable Φ is monotone as a function of $\boldsymbol{x}$ at time $\boldsymbol{t}$, it should be monotone at all consecutive times. For an arbitrary unstructured grid, this may be formulated: if $(\mathrm{grad}\,\Phi)_f^n \cdot \boldsymbol{d} \geq 0$ for all f, then $(\mathrm{grad}\,\Phi)_f^{n+m}\cdot \boldsymbol{d} \geq 0$ for all f and $m \geq 1$ (Ref. 34). For instance, for a method satisfying this criterion, oscillations cannot arise near an isolated propagating discontinuity. Another useful and frequently used constraint on numerical methods

is based on total variation (TV) stability, which for any conservative and consistent method is enough to guarantee convergence, i.e., $\inf\|\Phi^n - \omega\|_{1,T} \to 0$ as $\Delta t \to 0$, where ω is a weak solution to the governing equation of Φ and $\|\cdot\|_{1,T}$ is a 1-norm over a finite time interval [0, T] (Ref. 35). In the case of an arbitrary unstructured grid, the TV may be defined by

$$\mathrm{TV}(\Phi^n) = \sum_f \left|(\mathrm{grad}\,\Phi)_f^n \cdot \boldsymbol{d}\right|$$

The class of total variation diminishing (TVD) methods is based on the requirement that the TV is nonincreasing as time evolves, so that the TV is uniformly bounded by the TV of the initial data, i.e., $\mathrm{TV}(\Phi^{n+1}) \le \mathrm{TV}(\Phi^n)$, or more precisely

$$\sum_f \left|(\mathrm{grad}\,\Phi)_f^{n+1} \cdot \boldsymbol{d}\right| \le \sum_f \left|(\mathrm{grad}\,\Phi)_f^n \cdot \boldsymbol{d}\right|$$

From these definitions it is evident that the appearance of oscillations increases the TV, and by finite-domain-of-dependence arguments, we may conclude that any TVD method is also monotonicity preserving.

In contrast with the global constraints imposed by TVD methods, weaker constraints result from requiring that a dependent variable Φ should be instantaneously and locally monotone as a function of $\boldsymbol{x}$. Because of their inherently less diffusive nature, local monotonicity contraints appear to be more attractive choices in developing MILES schemes. For a structured grid, local monotonicity constraints can be derived from the convective boundedness criterion (CBC), first introduced by Gaskell and Lau,[36] proposing that $\Phi_{ij-1k} \le \Phi_{ijk} \le \Phi_{ij+1k}$. A generalization of this procedure to arbitrary unstructured grids has been derived by Darwish,[37] which may be improved by using gradients of the dependent variable so that, if the normalized variable is defined by $\vartheta_P = 1 - \frac{1}{2}[(\mathrm{grad}\,\Phi)_f \cdot \boldsymbol{d}]/[(\mathrm{grad}\,\Phi)_P \cdot \boldsymbol{d}]$, the CBC becomes $0 \le \vartheta_P \le 1$. This can be reinterpreted in the normalized variable (NV) diagram[36] displaying ϑ_f as a function of ϑ_P. Thus, for $0 \le \vartheta_P \le 1$, ϑ_P is bounded below by the function $\vartheta_f = \vartheta_P$ and above by unity, and it passes through the points (0, 0) and (1, 1); for $\vartheta_P < 0$ and $\vartheta_P > 1$, ϑ_f is equal to ϑ_P.

Figure 1a shows representative basic convective flux functions on the NV diagram. It is evident that only first-order (upwind) methods ensure local and instantaneous monotonicity, although being far too diffusive, whereas second- or higher-order methods are less diffusive but susceptible to nonlinear oscillations, which is manifested in their inability to preserve monotone profiles, cf., Godunov.[32] A strong candidate for the low-order numerical flux function used in Eq. (4) or (5) is, therefore, the first-order accurate upwind method of Courant et al.[38] The concept of normalized variables and the associated NV diagram provides us with a tool with which we can investigate the ability of numerical flux functions to ensure local and instantaneous monotonicity. Figure 1b shows selected convective flux functions that can be cast into form (4) or (5) based on the following different flux limiters: 1) the minmod limiter $\Gamma = \max[0, \min(1, 2r)]$, where $r = \vartheta_P^{-1} - 1$ (Ref. 34); 2) the van Leer limiter $\Gamma = (|r| + r)/(1 + |r|)$ (Ref. 39); 3) the superbee limiter $\Gamma = \frac{1}{2}\max[0, \min(2r, 1), \min(r, 2)]$ (Ref. 39); 4) the FCT limiter[33]; and 5) the gamma limiter $\Gamma = \frac{1}{2}[(1 - \vartheta_P/k)\mathrm{sgn}(\vartheta_P - k) + (\vartheta_P/k)\mathrm{sgn}\,\vartheta_P - \mathrm{sgn}(\vartheta_P - 1)]$ (Ref. 40), for which a recommended value is $k \approx 0.1$ and being fully TVD conservative for $k = 0.5$. All of these limiters satisfy the conditions for local and instantaneous monotonicity, but only the minmod and superbee limiters are TVD conformative, indicating that convective flux functions based on the latter are more diffusive than convective flux functions based on the FCT or gamma limiters; in addition, only the FCT and gamma limiters provide a smooth transition between $\tilde{f}_f^H$ and $\tilde{f}_f^L$.

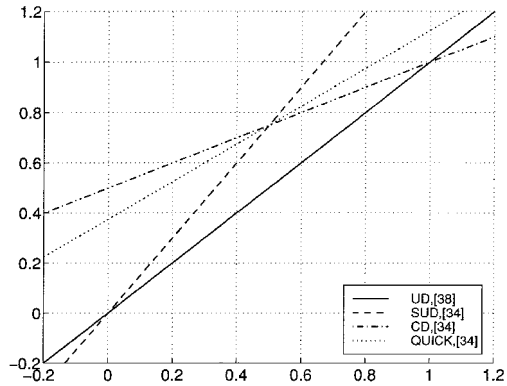

a) NVD diagram without flux limiters

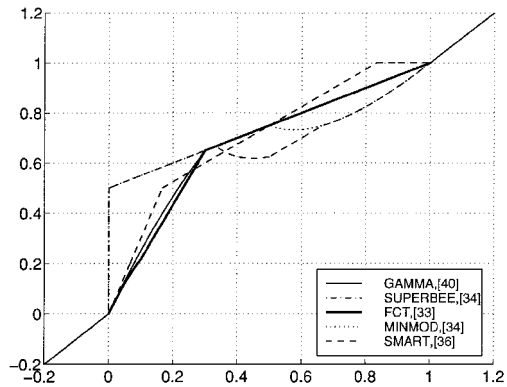

b) NVD diagram with flux limiters

Fig. 1 Boundedness or monotonicity criterion in the NV diagram for different functional reconstruction methods for the convective flux functions.

Explicit and Implicit SGS Turbulence Models

In the conventional LES, SGS models are explicitly introduced for closure in the low-pass filtered NSE (1), whereas in MILES, the effects of the SGS flow physics on the GS flow are included into the convective flux functions. In what follows, the modified equations from both approaches will be analyzed. To facilitate this investigation we focus on comparing two models: 1) a conventional LES model, discretized according to Eq. (2), using three-point backward time integration, a first-order functional reconstruction for the convective fluxes, and central difference approximations of the inner gradients in the combined fluxes and an ordinary eddy-viscosity model[3] and 2) a MILES model, discretized according to Eq. (3), also using three-point backward time integration, convective flux functions based on Eq. (5), where the high-order convective flux functions use first-order functional reconstruction and the low-order convective flux functions use upwind differencing, and central difference approximations of the inner gradients in the viscous fluxes. The main difference between the LES and MILES models lies in the treatment of the convective flux functions and the use of explicit eddy-viscosity-type SGS models for the conventional LES model.

For conventional LES, the modified equations are derived from Eq. (2) and the successive replacement of the chosen convective and combined flux functions and difference formulas by higher-order flux functions, difference formulas, and the corresponding leading-order truncation errors. Similarly, the time integration is replaced by the Crank–Nicholson method. Hence,

$$\partial_t(\bar{\rho}) + \mathrm{div}(\bar{\rho}\tilde{\boldsymbol{v}}) = \tfrac{1}{3}\Delta t_t^3 \partial_t(\bar{\rho}) + \mathrm{div}(\mathsf{G}\,\mathrm{grad}(\mathrm{grad}\,\bar{\rho})) + \cdots \quad (6a)$$

$$\partial_t(\bar{\rho}\tilde{\boldsymbol{v}}) + \mathrm{div}(\bar{\rho}\tilde{\boldsymbol{v}}) \otimes \tilde{\boldsymbol{v}} = -\mathrm{grad}\,\bar{p} + \mathrm{div}(\bar{\boldsymbol{S}} - \boldsymbol{B}) + \bar{\rho}\tilde{\boldsymbol{g}} + \tfrac{1}{3}\Delta t^2 \partial_t^3(\bar{\rho}\tilde{\boldsymbol{v}}) + \mathrm{div}(\bar{\rho}[\mathsf{G}\,\mathrm{grad}(\mathrm{grad}\,\boldsymbol{v})]) + \mathrm{div}(\mu \boldsymbol{G}\,\mathrm{grad}(\mathrm{div}(\mathrm{grad}\,\tilde{\boldsymbol{v}}))) + \cdots \quad (6b)$$

$$\partial_t(\bar{\rho}\tilde{e}) + \mathrm{div}(\bar{\rho}\tilde{\boldsymbol{v}}\tilde{e}) = \mathrm{div}(\bar{\boldsymbol{h}} - \boldsymbol{b}) - \bar{p}\,\mathrm{div}\,\tilde{\boldsymbol{v}} + \bar{\boldsymbol{S}} \cdot \tilde{\boldsymbol{D}} + \pi + \varepsilon + \bar{\rho}\tilde{\sigma} + \tfrac{1}{3}\Delta t_t^3 \partial_t(\bar{\rho}\tilde{e}) + \mathrm{div}(\bar{\rho}\mathsf{G}\,\mathrm{grad}(\mathrm{grad}\,\tilde{e})) + \mathrm{div}(\kappa \boldsymbol{G}\,\mathrm{grad}(\mathrm{div}(\mathrm{grad}\,e))) + \cdots \quad (6c)$$

where $\mathsf{G} = \frac{1}{6}(\boldsymbol{d} \otimes \boldsymbol{d} \otimes \boldsymbol{v})$, $\boldsymbol{G} = \frac{1}{12}(\boldsymbol{d} \otimes \boldsymbol{d})$, and [ ] represents the symmetrization operator. Hence, the leading-order truncation error is of $\mathcal{O}(\Delta t^2, |\boldsymbol{d}|^2)$ and for small Courant numbers (typical of LES and DNS) the transient contribution can be neglected, which indicates

that second-order dispersion and third-order dissipation dominate. Similar treatment of the MILES Eqs. (3) and (5) yields

$$\partial_t(\rho) + \operatorname{div}(\rho \boldsymbol{v}) = \tfrac{1}{3}\Delta t_t^3 \partial_t(\rho) + \operatorname{div}(\mathsf{G}\operatorname{grad}(\operatorname{grad}\rho)) + \cdots \quad (7a)$$

$$\begin{aligned}\partial_t(\rho \boldsymbol{v}) + \operatorname{div}(\rho \boldsymbol{v}\otimes\boldsymbol{v}) &= -\operatorname{grad} p + \operatorname{div}\boldsymbol{S} + \rho\boldsymbol{g} + \tfrac{1}{3}\Delta t^2 \partial_t^3(\rho \boldsymbol{v}) \\ &+ \operatorname{div}(\rho(\boldsymbol{v}\otimes\boldsymbol{r} + \boldsymbol{r}\otimes\boldsymbol{v} + \boldsymbol{r}\otimes\boldsymbol{r}) + \rho[\mathsf{G}\operatorname{grad}(\operatorname{grad}\boldsymbol{v})]) \\ &+ \operatorname{div}(\mu \boldsymbol{G}\operatorname{grad}(\operatorname{div}(\operatorname{grad}\boldsymbol{v}))) + \cdots \end{aligned} \quad (7b)$$

$$\begin{aligned}\partial_t(\rho e) + \operatorname{div}(\rho \boldsymbol{v} e) &= \operatorname{div}\boldsymbol{h} - p\operatorname{div}\boldsymbol{v} + \boldsymbol{S}\cdot\boldsymbol{D} + \rho\sigma \\ &+ \tfrac{1}{3}\Delta t_t^3 \partial_t(\rho e) + \operatorname{div}(\rho r \boldsymbol{v} + \rho\mathsf{G}\operatorname{grad}(\operatorname{grad} e)) \\ &+ \operatorname{div}(\kappa \boldsymbol{G}\operatorname{grad}(\operatorname{div}(\operatorname{grad} e))) + \cdots \end{aligned} \quad (7c)$$

where $\boldsymbol{r} = \beta\,(\operatorname{grad}\boldsymbol{v})\boldsymbol{d}$, $r = \beta\,(\operatorname{grad} e\cdot\boldsymbol{d})$, and $\beta = \frac{1}{2}(1-\Gamma)\,\operatorname{sgn}((\boldsymbol{v}\cdot\boldsymbol{d})/|\boldsymbol{d}|)$. Thus, the leading-order truncation error is of $\mathcal{O}(\Delta t^2, |\boldsymbol{d}|)$, and for small Courant numbers first-order dissipation dominates if $\Gamma \neq 1$, i.e., in points where the flux limiter is activated; otherwise, second-order dispersion and third-order dissipation dominate so that the leading-order truncation error is of $\mathcal{O}(\Delta t^2, |\boldsymbol{d}|^2)$.

Comparison of the modified equations from the LES model (6) with the modified equations from the MILES model (7) implies that the leading-order truncation error in the MILES model may formally replace the explicit SGS model in the conventional LES model. In MILES, we may, thus, interpret the leading-order truncation error as implicit, or built-in SGS models, i.e.,

$$\boldsymbol{B} = -\rho(\boldsymbol{v}\otimes\boldsymbol{r} + \boldsymbol{r}\otimes\boldsymbol{v} + \boldsymbol{r}\otimes\boldsymbol{r}), \qquad \boldsymbol{b} = -\rho(r\boldsymbol{v}) \quad (8)$$

with their behavior being governed by the flux limiter and its intrinsic properties. Note that the term $\pi + \varepsilon$ in the conventional LES model (6) does not have a true counterpart in the MILES model unless it is lumped into the SGS flux. To facilitate the following discussion we may rewrite Eq. (8) as

$$\begin{aligned}\boldsymbol{B} &= -\rho\{\beta[(\boldsymbol{v}\otimes\boldsymbol{d})(\operatorname{grad}\boldsymbol{v})^T + (\operatorname{grad}\boldsymbol{v})(\boldsymbol{v}\otimes\boldsymbol{d})^T] \\ &+ \beta^2(\operatorname{grad}\boldsymbol{v})\boldsymbol{d}\otimes(\operatorname{grad}\boldsymbol{v})\boldsymbol{d}\} = -\rho(\boldsymbol{C}\boldsymbol{L}^T + \boldsymbol{L}\boldsymbol{C}^T + \beta^2\boldsymbol{L}\boldsymbol{d}\otimes\boldsymbol{L}\boldsymbol{d}) \end{aligned} \quad (9a)$$

$$\boldsymbol{b} = -\rho\beta(\boldsymbol{v}\otimes\boldsymbol{d})\operatorname{grad} e = -\rho\boldsymbol{C}\operatorname{grad} e \quad (9b)$$

where $\boldsymbol{C} = \beta(\boldsymbol{v}\otimes\boldsymbol{d})$ and $\boldsymbol{L} = \operatorname{grad}\boldsymbol{v}$. The expressions for $\boldsymbol{B}$ and $\boldsymbol{b}$ are of a more general tensorial form than those of the eddy-viscosity expressions used in the conventional LES models. Here, the SGS stress tensor consists of two terms: $\boldsymbol{B}^{(1)} = -\rho(\boldsymbol{C}\boldsymbol{L}^T + \boldsymbol{L}\boldsymbol{C}^T)$ and $\boldsymbol{B}^{(2)} = -\rho\beta^2\boldsymbol{L}\boldsymbol{d}\otimes\boldsymbol{L}\boldsymbol{d}$, of which the former is a generalized eddy-viscosity model with $\boldsymbol{C}$ being a second-rank eddy-viscosity tensor and the latter is of a form similar to that originally suggested by Leonard.[41] The term $\boldsymbol{B}^{(2)}$ is also essentially equivalent to the representation of $\boldsymbol{B}$ in the scale-similarity model of Bardina et al.,[42] which often is used together with an eddy-viscosity model in a mixed model.[29] Recently, Borue and Orszag[43] examined some statistical properties of the SGS stress tensor, the local energy flux and the velocity gradients, and concluded that a tensorial term of the form $\boldsymbol{B}^{(2)}$ greatly improved the correlations between the exact and modeled SGS stress tensor. The functional form of Eq. (9a) also permits the eigenvectors of $\boldsymbol{B}$ to be different from those of $\boldsymbol{D}$, possibly alleviating some of the limitations of the scalar-valued eddy-viscosity model $\boldsymbol{B} = \frac{2}{3}\rho k\boldsymbol{I} - \mu_k(\boldsymbol{L}+\boldsymbol{L}^T)$. To facilitate comparison of different SGS models, we introduce an equivalent scalar-valued viscosity by contracting $\boldsymbol{B}$ with the rate-of-strain tensor $\boldsymbol{D}$ so that $\mu^* = \frac{1}{2}\boldsymbol{B}\cdot\boldsymbol{D}/\|\boldsymbol{D}\|^2$. Furthermore, the frame indifference requirements imply that $\boldsymbol{B}$ (and $\boldsymbol{b}$) should be frame indifferent; because $\tilde{\boldsymbol{v}}^* = \dot{\boldsymbol{c}} + \boldsymbol{Q}\tilde{\boldsymbol{v}} + \dot{\boldsymbol{Q}}\tilde{\boldsymbol{x}}$, it follows that $\tilde{\boldsymbol{L}}^* = \boldsymbol{Q}\tilde{\boldsymbol{L}}\boldsymbol{Q}^T + \dot{\boldsymbol{Q}}\boldsymbol{Q}^T$ and $\boldsymbol{d}^* = \boldsymbol{Q}\boldsymbol{d}$. From this it is apparent that neither $\boldsymbol{b}$ nor $\boldsymbol{B}$ is frame indifferent. However, it can be verified that these are invariant under the Galilean group of transformations.[25] Moreover, to determine the necessary physics that should be built into the flux limiter, we may consider the necessary and sufficient conditions for $\boldsymbol{B}\in P\text{sym}$ resulting in the inequalities

$$\boldsymbol{C}\cdot\boldsymbol{L} + \beta \mid \boldsymbol{L}\boldsymbol{d}^2 \geq 0 \quad (10a)$$

$$\tfrac{1}{4}[\boldsymbol{C}\cdot\boldsymbol{L} + \beta \mid \boldsymbol{L}\boldsymbol{d}^2]^2 \geq \operatorname{tr}[(\boldsymbol{C}\boldsymbol{L}^T + \boldsymbol{L}\boldsymbol{C}^T + \beta\boldsymbol{L}\boldsymbol{d}\otimes\boldsymbol{L}\boldsymbol{d})^2] \quad (10b)$$

$$\beta^3\det(\boldsymbol{C}\boldsymbol{L}^T + \boldsymbol{L}\boldsymbol{C}^T + \beta\boldsymbol{L}\boldsymbol{d}\otimes\boldsymbol{L}\boldsymbol{d}) \leq 0 \quad (10c)$$

These constraints may be satisfied by a suitable choice of Γ; i.e., existing flux limiters can be investigated in the light of Eq. (10), or alternative limiters can be explored using Eq. (10) in conjunction with conventional numerical considerations. For an arbitrary flux limiter, the implicit SGS model does not satisfy all constraints imposed by frame indifference, realizability, symmetry, and non-negative dissipation of SGS kinetic energy, but by some choice of Γ, these constraints may be satisfied.

Forced Homogeneous Isotropic Turbulence

For homogeneous isotropic turbulence, the specific body force $\boldsymbol{g}$ can be used to create random forcing of the large-scale motion. The forcing must maintain a steady spectrum and allow the collection of statistical correlations. Several forcing schemes have previously been adopted for this purpose, cf., Ref. 44; however, because we need to represent particular length scales and velocity distributions corresponding to the DNS data of Jiménez et al.,[15] a more versatile method is needed. Here, the forcing scheme of Eswaran and Pope[45] is used, in which $\boldsymbol{g}(\boldsymbol{k}, t) = P(\boldsymbol{k})\boldsymbol{w}(\boldsymbol{k}, t)[\Theta(\boldsymbol{k}) - \Theta(\boldsymbol{k}-\boldsymbol{k}_F)]$, where Θ is the step function, $P(\boldsymbol{k}) = \boldsymbol{I} - |\boldsymbol{k}|^{-2}(\boldsymbol{k}\otimes\boldsymbol{k})$, and $\boldsymbol{w}(\boldsymbol{k}, t)$ is a vector-valued Uhlenbeck–Ornstein process characterized by $\langle \boldsymbol{w}(\boldsymbol{k}, t)\otimes\boldsymbol{w}^*(\boldsymbol{k}, t+s)\rangle = 2\sigma^2\exp(-s/\tau)\boldsymbol{I}$ in the equilibrium limit. Four parameters are introduced: the amplitude σ, the timescale τ, and the wave numbers k_L and k_F. The statistical properties of the turbulence can be influenced by the features of the driving; however, values for k_L and k_F are selected so that only the largest scales are driven. The initial velocity field is given by superimposing Fourier modes having a prescribed energy spectrum but random phases.

The numerical methods used here are based on Eqs. (2) and (3), but with the continuity Eqs. (2a) and (3a) replaced by discrete Poisson equations for pressures $\bar{p}$ and p depending on if the conventional LES model or the MILES model is used. To guarantee conservation of mass, the momentum Eqs. (2b) and (3b) are solved for $\tilde{\boldsymbol{v}}_P^{n+m}$ and $\boldsymbol{v}_P^{n+m}$, the face interpolates of which are used to calculate the face fluxes $\tilde{F}_f = (\tilde{\boldsymbol{v}}\cdot\mathrm{d}\boldsymbol{A})_f$ and $F_f = (\boldsymbol{v}\cdot\mathrm{d}\boldsymbol{A})_f$. Eliminating the face interpolates $\tilde{\boldsymbol{v}}_f^{n+m}$ and $\boldsymbol{v}_f^{n+m}$ between Eq. (2a) and $\tilde{\boldsymbol{v}}_P^{n+m}$ and between Eq. (3a) and $\boldsymbol{v}_P^{n+m}$ results in discretized Poisson equations, which for the conventional LES model (2) implies that Eq. (2a) is replaced by

$$\begin{aligned}&\sum_f\left\{\left(a_P^{-1}\right)_f\left[\operatorname{grad}(\bar{p})_f^{n+m}\cdot\mathrm{d}\boldsymbol{A}\right]\right\} \\ &= \sum_f\left(\left\{a_P^{-1}\left[\sum_{i=0}^{m}\sum_N\left(a_N^{n+i}\tilde{\boldsymbol{v}}_N^{n+i}\right)\right.\right.\right. \\ &\left.\left.\left.+\sum_{i=0}^{m-1}\left(b_p^{n+i}\tilde{\boldsymbol{v}}_P^{n+i}\right)\right]\right\}_f\cdot\mathrm{d}\boldsymbol{A}\right)\end{aligned} \quad (11)$$

and for the MILES model (3) this implies that Eq. (3a) is replaced by

$$\begin{aligned}&\sum_f\left\{\left(a_P^{-1}\right)_f\left[\operatorname{grad}(p)_f^{n+m}\cdot\mathrm{d}\boldsymbol{A}\right]\right\} \\ &= \sum_f\left(\left\{a_P^{-1}\left[\sum_{i=0}^{m}\sum_N\left(a_N^{n+i}\boldsymbol{v}_N^{n+i}\right)\right.\right.\right. \\ &\left.\left.\left.+\sum_{i=0}^{m-1}\left(b_p^{n+i}\boldsymbol{v}_P^{n+i}\right)\right]\right\}_f\cdot\mathrm{d}\boldsymbol{A}\right)\end{aligned} \quad (12)$$

where a_P, a_N, and b_P are matrix coefficients. The discretized equations, $\tilde{\boldsymbol{U}}_P^{n+m} = \boldsymbol{H}(\tilde{\boldsymbol{U}}_P^{n+i};\,\mu,\, i\in[1,m])$ and $\boldsymbol{U}_P^{n+m} = \boldsymbol{H}(\boldsymbol{U}_P^{n+i};\,\mu,\, i\in[1,m])$, where $\tilde{\boldsymbol{U}} = [\bar{p}, \tilde{\boldsymbol{v}}, \tilde{e}]^T$ and $\boldsymbol{U} = [p, \boldsymbol{v}, e]^T$, respectively, are solved using a segregated approach leading to a Courant number restriction; it is found that a maximum Courant number of 0.2 gives satisfactory numerical stability and temporal accuracy.

LES has been carried out for two Taylor Reynolds numbers, $Re_T = 96$ and 305, corresponding to bulk Reynolds numbers of $\mathcal{O}(5 \times 10^3)$ and $\mathcal{O}(50 \times 10^3)$, respectively, using two conventional LES models and two MILES models. In the first LES model we use the SMG model, resulting in the effective viscosity $\mu_{\text{eff}} = \mu + c_D \bar{\rho} \Delta^2 \|\tilde{\boldsymbol{D}}\|$, where $c_D = 0.02$, and in the second we use the dynamic SMG model (DSMG)[4] in which the model coefficient c_D is evaluated dynamically using information from the resolved flow. To prevent numerical ill conditioning in the DSMG, the nominator and denominator in the expression for the dynamic model coefficient are averaged over homogeneous directions, in essence removing the spatial dependence of the coefficient so that $c_D = c_D(t)$. The choice of LES models is based on a previous study,[12] and they are selected to be representative of simple and well-documented models applicable to engineering problems in complex geometries, as well as state-of-the-art models. The first MILES model is based on the Euler equations (MILES-EU), i.e., we consider only convection and assume that the flow can be regarded as virtually inviscid and isothermal so that $\mu_{\text{eff}} = \mu_k$, where μ_k is the scalar-valued characteristic viscosity of the FCT scheme; in the second model (MILES), we include the molecular viscosity so that $\mu_{\text{eff}} = \mu + \mu_k$, but we neglect thermal effects, taking advantage of the virtually isothermal nature of the flow.

Figures 2a and 2b show the mean energy spectra $E = E(|\boldsymbol{k}|)$ for $Re_T = 96$ and 305, respectively, together with the Driscoll and Kennedy (DK) spectrum[46] and, for $Re_T = 96$, the DNS energy spectrum of Jiménez et al.[15] after about 10 eddy turnover times. Wave numbers are nondimensionalized with grid wave number, and nondimensionalization of the energy density involves the mean energy dissipation rate computed in the simulations. The energy spectra are based on averaging over 25 spectra evaluated at instants well separated in time so that they can be considered statistically independent. In addition, it has been verified that there is no monotonic trend in the GS or SGS kinetic energy and so we may assume that a statistically steady state has been attained. To confirm that without (explicit or implicit) SGS models the energy decay is not well captured, simulations without such models, so-called underresolved DNS (UDNS), (using central-difference convection discretization) were performed on both the 32^3 and 64^3 grids. Figure 2a shows that the slope of the energy spectra for UDNS near the end of the inertial subrange is too low, so that energy tends to accumulate at the higher wave numbers. This indicates that the presence of an adequate (implicit or explicit) SGS model is required to ensure the correct distribution of energy on the grid scales. It also demonstrates that numerical diffusion from the central-difference convection discretization is negligible in comparison to the diffusion of the SGS models considered.

For the $Re_T = 96$ case (shown in Fig. 2a) having only a short inertial range, the energy spectra are found to depend on the effects of the SGS model only toward the high-wave-number end of the inertial range and into the viscous subrange, which is in contrast to the energy spectra resulting from UDNS. All LES models, irrespective of SGS model and the spatial resolution, appear to reproduce the low-wave-number part and the inertial range of the spectrum satisfactorily, and no significant differences between the different SGS models can be detected using this information. The spectra from the 32^3 LES end near the high-wave-number end of the inertial subrange, indicating that only a small fraction of the kinetic energy is within the unresolved flow (Table 1). Toward the high-wave-number end of the energy spectra, i.e., for $\lambda_I |\boldsymbol{k}| \geq 6$, viscous effects begin to emerge in the 64^3 LES, so that the decay of $E(|\boldsymbol{k}|)$ increases at about the same rate as does the DNS spectrum until the spectra abruptly expire. For the 64^3 resolution, about 98% of the total kinetic energy is within the resolved flow. Results from the $Re_T = 305$ case, identified by a well-developed inertial subrange (as evident from Fig. 2b), suggest that, for the 32^3 LES, around 20% of the kinetic energy resides within the unresolved scales, and for the 64^3 LES this amount decreases to about 12% (Table 1). Although all LES models investigated were found to reproduce the Driscoll and Kennedy[46] spectrum reasonably well, some differences may be detected. In particular, it should be observed that both MILES and MILES-EU underpredict the magnitude of the energy spectra at the coarse 32^3 resolution, whereas both SMG and DSMG still give good results. However, all models predict the slope of the energy spectra well so that it coincides with the expected $k^{-5/3}$ slope, as found in the DK[46] spectrum. For the 64^3 resolution all models behave equally well.

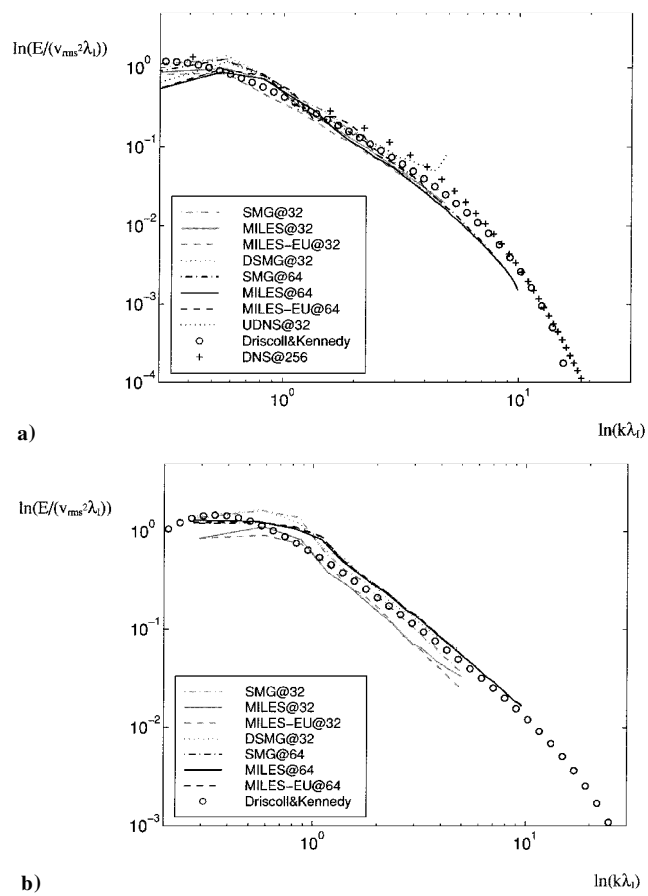

Fig. 2 Large-scale normalized energy spectra from different LES models at a) $Re_T = 96$ and b) $Re_T = 305$ compared to spectra from DNS[15] and from the theoretical spectra of Driscoll and Kennedy.[46]

Table 1 Nominal parameters for the forced homogeneous isotropic turbulence cases

Simulation	Grid	Re_T	λ_I, m	λ_I, m	$\lvert\langle \boldsymbol{v}_{\text{rms}} \rangle\rvert$, m/s	$k/\langle k \rangle^{\text{a}}$	$\varepsilon/\langle \varepsilon \rangle^{\text{a}}$
DNS[15]	256^3	96	1.37	0.312	0.61	——	——
SMG	$32^3(64^3)$	96(95)	1.41(1.39)	0.314(0.316)	0.57(0.56)	0.04(0.04)	0.50(0.51)
DSMG	$32^3(64^3)$	95(96)	1.39(1.38)	0.316(0.315)	0.56(0.57)	0.04(0.04)	0.50(0.51)
MILES-EU	$32^3(64^3)$	94(95)	1.33(1.31)	0.312(0.309)	0.54(0.56)	0.03(0.03)	0.48(0.50)
MILES	$32^3(64^3)$	95(96)	1.36(1.36)	0.312(0.311)	0.57(0.57)	0.04(0.04)	0.50(0.51)
SMG	$32^3(64^3)$	305(304)	1.71(1.72)	0.232(0.234)	2.49(2.46)	0.21(0.18)	3.12(3.01)
DSMG	$32^3(64^3)$	303(303)	1.69(1.71)	0.233(0.236)	2.46(2.43)	0.23(0.17)	3.17(2.67)
MILES-EU	$32^3(64^3)$	307(305)	1.65(1.75)	0.225(0.232)	2.48(2.47)	0.16(0.17)	3.11(2.15)
MILES	$32^3(64^3)$	305(306)	1.73(1.72)	0.232(0.233)	2.49(2.48)	0.20(0.14)	3.11(3.11)

[a]Estimates of $k/\langle k \rangle$ and $\varepsilon/\langle \varepsilon \rangle$ are based on evaluating the integrals defining k and e using DNS data or the DK spectra, depending on turbulent Reynolds number over the unresolved part of the wave number range.

Based on the energy spectra, we can evaluate the following characteristic flow quantities: the rms-velocity fluctuations $v_{\rm rms} = \langle(\tilde{\boldsymbol{v}} - \langle\tilde{\boldsymbol{v}}\rangle)^2\rangle^{1/2}$, the Taylor microscale $\lambda_T = (\langle v_{\rm rms}^2\rangle / \langle\|\tilde{\boldsymbol{L}}\|^2\rangle)^{1/2}$, the mean kinetic energy

$$\langle k\rangle = \frac{1}{2}\langle \boldsymbol{v}^2\rangle = \int_0^\infty E(\boldsymbol{k}, t)\,\mathrm{d}\boldsymbol{k} = \frac{1}{2}\langle\tilde{\boldsymbol{v}}^2\rangle + k$$

where $\frac{1}{2}\langle\tilde{\boldsymbol{v}}^2\rangle$ is the resolvable kinetic energy and k is the SGS kinetic energy, and the mean effective dissipation rate

$$\langle\varepsilon\rangle = 2\nu\langle\|\boldsymbol{D}\|^2\rangle = 2\nu\int_0^\infty \boldsymbol{k}^2 E(\boldsymbol{k}, t)\,\mathrm{d}\boldsymbol{k} = 2\nu\langle\|\tilde{\boldsymbol{D}}\|^2\rangle + \varepsilon$$

where ε is the SGS dissipation and $2\nu\langle\|\tilde{\boldsymbol{D}}\|^2\rangle$ is the resolvable dissipation. Comparison of these integral quantities in Table 1 shows that they are well reproduced by all LES models.

To clarify the relative importance of the SGS models on the macroscopic flow structures, cumulative distribution functions (CDFs) of the resolvable vorticity magnitude $|\tilde{\boldsymbol{\omega}}|$ are shown in Figs. 3a and 3b for $Re_T = 96$ and 305, respectively. For comparison purposes, these are overlaid with CDFs of the raw vorticity magnitude $|\boldsymbol{\omega}|$ from the DNS studies of Jiménez et al.[15] Because there is no other comparable data at $Re_T = 305$, we have chosen to include the DNS data at $Re_T = 168$ (highest Reynolds number available) as suitable reference in Fig. 3b. The CDFs represent the volume fraction occupied by values of a quantity above a given threshold level. To enhance the difference in performance between SGS models, as well as the deviation from DNS, Fig. 3 presents the CDFs in semilogarithmic format. Note that the tails contain only small fractions of the total volume, and if these diagrams were to be presented in linear format, then LES and DNS results would appear virtually indistinguishable. It is also clear that the LES mesh resolution used here is not fine enough to capture the small-scale, high-intensity vortical structures embedded in the weaker vorticity background of lower intensity. In support of this, we observe that the 64^3 LES displays longer tails than the 32^3 LES but still shorter tails than the DNS. Moreover, there seems to be a significant spread in the predictions of $|\tilde{\boldsymbol{\omega}}|$ depending on the SGS model used; at $Re_T = 96$, DSMG shows the best agreement with DNS data at the 32^3 resolution, whereas MILES shows the best agreement with DNS data at the 64^3 resolution. At $Re_T = 305$ the spread appears to be larger, in particular for the lower resolution, and again the same models show the best agreement with DNS data at both resolutions. From these results it appears that the predictive capability of the MILES model is more sensitive to spatial resolution than conventional LES, e.g., using SMG. On the other hand, the MILES-EU model performs well on both resolutions. This difference may reflect on the lack of molecular viscosity with MILES-EU, for which lower overall effective viscosity is thus involved. The distributions of $|\tilde{\boldsymbol{\omega}}|$ are far from Gaussian, although the LES data are more Gaussian than the DNS data and display few signs of converging to a limit distribution for large turbulence Reynolds number. Most of $|\tilde{\boldsymbol{\omega}}|$ is contained in a weak background that would not affect low-order statistical moments, although it will dominate high-order moments.

For completeness, Fig. 4 shows the CDFs for the resolvable rate of strain $\|\tilde{\boldsymbol{D}}\|$ together with the raw rate of strain from the DNS of Jiménez et al.[15] Again, it is clear that the distributions are far from Gaussian, with the DNS data being less Gaussian than the LES data, and it is also clear that the DNS have a more pronounced tail than the LES data. As observed in Fig. 3, the mesh resolution in LES does not support the resolution of the intense flow structures associated with worm vortices. This is again supported by the longer tails of the 64^3 LES as compared to the 32^3 LES, both having shorter tails than the DNS. Also apparent from Figs. 3 and 4 is that the volume fractions of $|\tilde{\boldsymbol{\omega}}|$ in the unresolved structures are larger than in the corresponding volume fractions of $\|\tilde{\boldsymbol{D}}\|$. This suggests that the latter are associated with larger spatial scales than the former. From Figs. 3 and 4 we may

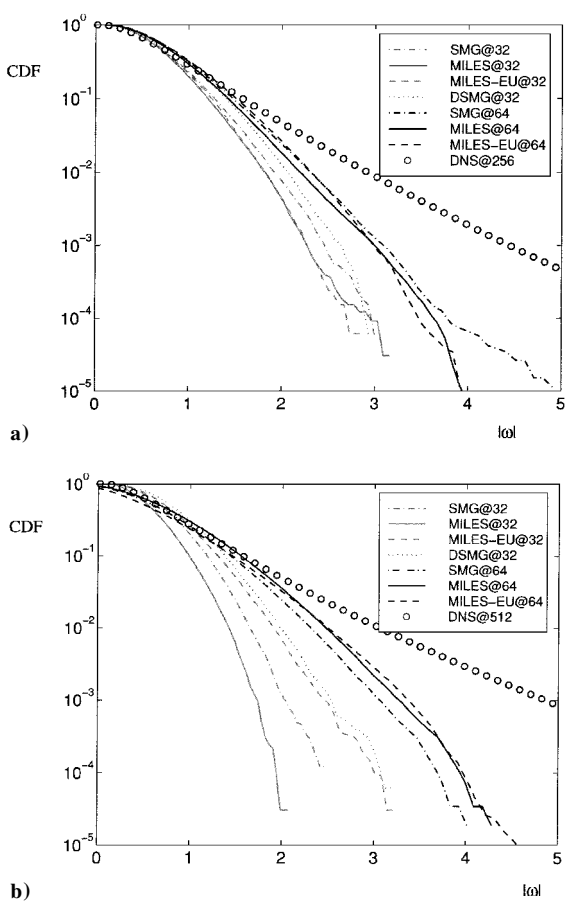

Fig. 3 CDFs of vorticity magnitude $|\tilde{\boldsymbol{\omega}}|$ for the various LES models overlaid with DNS data of Jiménez et al.[15]: a) $Re_T = 96$ and b) $Re_T = 305$. (Note that DNS data in this case correspond to $Re_T = 168$; cf. Ref. 15.)

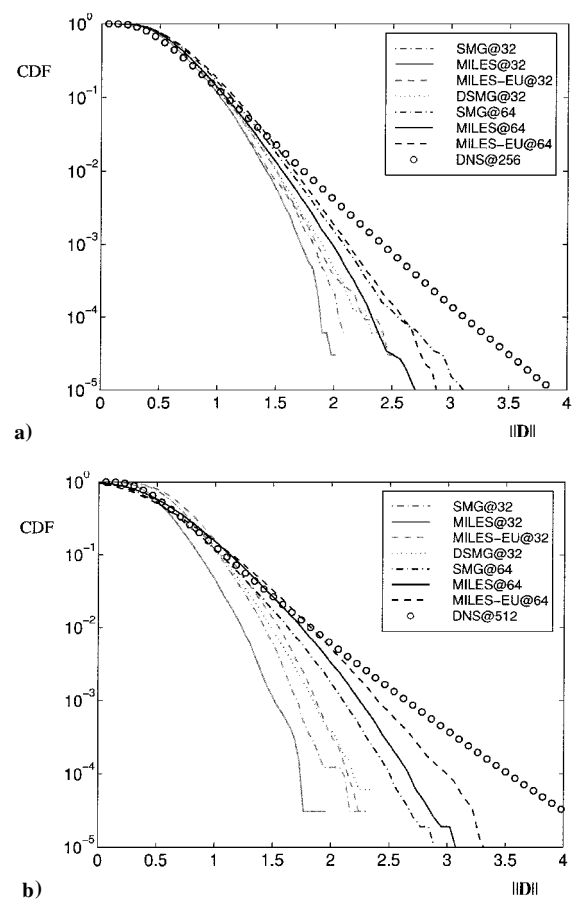

Fig. 4 CDFs of the rate of strain $\|\tilde{\boldsymbol{D}}\|$ for the various LES models overlaid with DNS data of Jiménez et al.[15]: a) $Re_T = 96$ and b) $Re_T = 305$. (Note that DNS data in this case correspond to $Re_T = 168$.)

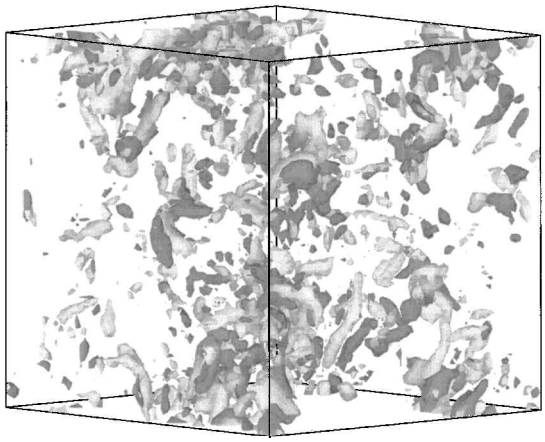

a) SMG at $Re_T = 305$

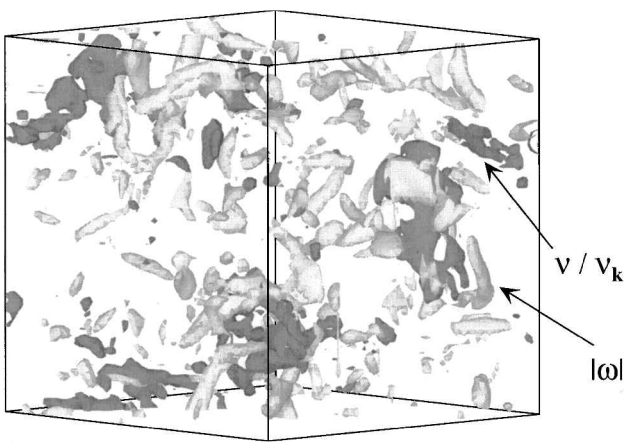

b) MILES at $Re_T = 305$

Fig. 5 Isosurfaces of the vorticity magnitude (lighter-shaded surfaces), with $|\tilde{\omega}| = \frac{3}{2}\langle|\tilde{\omega}|\rangle/\tilde{\omega}_{\rm rms}$ and SGS viscosity ν_k at $\nu_k/\nu = 3.0$.

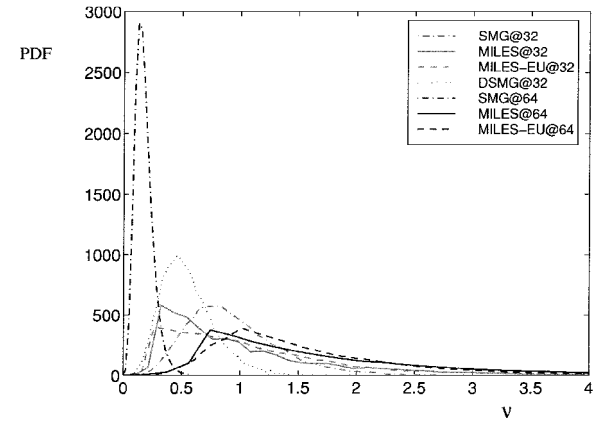

a) $Re_T = 96$

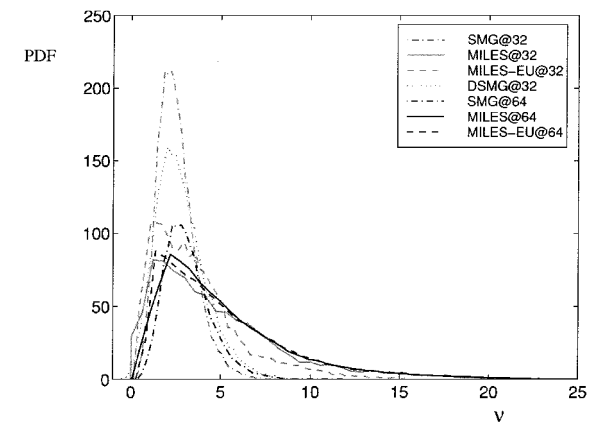

b) $Re_T = 305$

Fig. 6 PDFs of the explicit and implicit SGS viscosity ν_k, from the various LES models.

conclude that the concept of LES seems to be independent of the SGS model if it can smoothly channel the kinetic energy out of the wave numbers close to the cutoff wave number to prevent aliasing; hence, the SGS model must be active at the correct locations. The observation that the best agreement with DNS data is obtained with DSMG on the 32^3 resolution but with MILES on the 64^3 resolution is further corroborated by these results.

Figure 5 shows isosurfaces of $|\tilde{\omega}|$ at the level $|\tilde{\omega}| = \frac{3}{2}\langle|\tilde{\omega}|\rangle/\tilde{\omega}_{\rm rms}$ and the SGS viscosity $\nu_k = \mu_k/\rho$ at the level $\nu_k/\nu = 3.0$ for SMG and MILES at $Re_T = 305$. The particular values selected for the isosurfaces of ν_k correspond to the peaks in the probability density functions of the SGS viscosity, as shown in Fig. 6. Coherent vortical structures, sometimes referred to as fat worms, are present in the resolved flow independently of the SGS model. Such structures have been reported for LES of homogeneous isotropic turbulence,[47,48] and in DNS similar but thinner structures, worms, are often reported. Also, Vincent and Meneguzzi[49] have observed fat worms similar to those predicted by LES in filtered DNS data. Clearly, such worms cannot be properly resolved in LES and are, thus, replaced by fat worms, and it therefore appears reasonable that the observed presence of the coherent elongated vortices is a realistic prediction based on the exact or prefiltered NSE. Hence, $\tilde{\omega}$ appears in coherent filaments stretched and intensified by the resolved rate of strain $\tilde{\boldsymbol{D}}$. Although the different SGS models result in somewhat different CDFs $|\tilde{\omega}|$, of they all reproduce the correct behavior, with DSMG and MILES offering the best comparison with DNS at $Re_T = 96$. Most of the volume is occupied by relatively weak vorticity with strong vortices filling only a small fraction of the computational box. Of these, only a fraction have a diameter large enough to be resolved in LES. The structure of the resolved vorticity implies that weak and strong vortices have distinct topology; whereas there is no evident structure in the low-intensity regions, the high-intensity regions tend to be organized mostly in tubes. Such structures, which have a Gaussian radial distribution, are found to appear on the edges of regions that are almost uniform in velocity. Furthermore, similar to the situation in DNS, interferences between flow structures seem to create shear layers, which may roll up into vortex tubes.

The distribution of ν_k or $\nu^* = \mu^*/\rho$ for the MILES and MILES-EU models is of interest to differentiate between different LES models, but also to enhance our present understanding of the underlying physics. As indicated by Fig. 5, the spatial distribution of the SGS viscosity for MILES and a conventional LES model, such as SMG, are distinctly different. The MILES implicit SGS viscosity is found to be rather uncorrelated with the coherent structures, whereas for most conventional LES models the explicit SGS viscosity tends to peak between closely spaced tubular structures that are regions experiencing large strain and vortex stretching (see also Ref. 12). A positive SGS viscosity implies that energy is transferred from resolvable structures toward small unresolved structures via a cascade process (outscatter), whereas a negative SGS viscosity implies that energy is transferred in the opposite direction by a reverse cascade process, i.e., backscatter. Backscatter may become important when a large amount of turbulent kinetic energy is present in the unresolved scales, i.e., when the spatial resolution is marginal, as is usual when LES is applied to a more complex flow, which here is emulated with the lower spatial resolution. In addition, in these circumstances, anisotropy effects may also become increasingly important, and so the SGS models should be able to accomodate both flow and grid anisotropies.

In Fig. 6, instantaneous probability density functions (PDFs) of ν_k and ν^* at $Re_T = 96$ and 305 are shown normalized with the molecular viscosity ν. The SMG result in PDFs of similar shape but with different domains of dependence. More precisely, PDFs resulting from SMG are shifted toward higher values of the SGS viscosity, whereas PDFs from DSMG are shifted toward lower values of the SGS viscosity. In fact, a very small fraction of negative values of

the SGS viscosity, indicating backscatter, is observed for DSMG for both turbulence Reynolds numbers. The PDFs from the MILES models are found to be distinctly different: MILES-EU results in a narrow distribution of SGS viscosity, whereas MILES results in a wider distribution, similar to but narrower than that of the SMG model. From this we conclude that, although the generic form of SGS viscosity is the same for MILES-EU and MILES, the distribution of SGS viscosity is different. This difference is probably due to the presence of the molecular viscosity causing additional spreading of steep gradients, which in turn affects the flowfield.

MILES of Transitional Freejets

Next we focus on modeling the transition to turbulence in a free square jet evolving from laminar initial conditions. The jet is initialized with a thin square vortex sheet having slightly rounded-off corner regions and uniform initial momentum thickness.[22] This models the problem of a laminar jet emerging from a sharp-edged orifice nozzle, where the initial shear layers have virtually uniform zero momentum thickness and the sharpness of the jet corners is smoothed out immediately downstream of the nozzle due to diffusion. For such orifice jets, the role of boundary layers is minimal and is reduced to contributing to the definition of the thin vorticity thickness.

The three-dimensional jet model is based on the solution of the nonhomogeneous compressible NSE[24] using the equation of state for an ideal gas.[22] Inflow/outflow conditions are imposed at the open boundaries in the streamwise direction, and stagnant flow conditions are imposed at the cross-stream boundaries; inflow conditions modeling the initial (jet exit) conditions include specifying the mass density and velocities. Axial forcing is implemented to facilitate the analysis of the results by superimposing on the freejet velocity U_0 an axial, time-dependent, sinusoidal perturbation (2.5% rms of U_0). This weak axial forcing involves a nondimensional Strouhal frequency, $fD_e/U_0 = 0.5$ (consistent with observed jet preferred frequencies in laboratory experiments), where D_e is the jet equivalent diameter, defined as the diameter of a circular jet having the same cross-sectional area, i.e., $D_e = (2/\sqrt{\pi})D$, where D is the length of the sides of the square jet. The suitability of this jet simulation approach is supported by the very good agreement found between near-field growth rates of unforced experimental orifice jets with nearly laminar initial conditions and the corresponding growth rates of weakly excited jets such as investigated here.[21]

The Cartesian computational grids used in the computational studies reported here consist of evenly spaced cells in the shear flow region of interest. Geometrical stretching in the cross-stream direction outside of the latter region is used to implement the open boundary conditions. The grids are held fixed in time, with Courant–Friedrichs–Lewy number CFL = 0.5, and typically use between $120 \times 87 \times 87$ (grid C with a characteristic cell size of 2Δ) and $240 \times 174 \times 174$ (grid F with cell size Δ) computational cells. Simulations were also performed on an intermediate-resolution grid using $150 \times 110 \times 110$ cells (grid I with cell size 1.5Δ). The complete computational domain has a streamwise extent of approximately $7D_e$ and extends up to $\pm 5D_e$ away from the jet axis in the transverse directions.

The numerical methods used in the transitional jet simulations are based on splitting the integrations for streamwise convection, cross-stream convection, and other local processes (viscosity and thermal conduction) in the discretized Eqs. (2) and (3). Using this framework, the time integration is performed as $\boldsymbol{U}_P^{n+i} = \mathcal{S}[\mathcal{L}_{23}(\mathcal{L}_1 \boldsymbol{U}_P^n)]$, where $\boldsymbol{U} = [\rho, \rho\boldsymbol{v}, \rho e]^T$, and where the streamwise, cross-streamwise and localized operators $\mathcal{L}_1$, $\mathcal{L}_{23}$, and $\mathcal{S}$ are defined as follows:

$\mathcal{L}_1$:

$$\sum_{i=1}^{m} \left\{ \alpha_i \boldsymbol{U}_P^{n+i} + \frac{\beta_i \Delta t}{\delta V_P} \sum_{f:\boldsymbol{n}=\boldsymbol{e}_1} \left[\tilde{\boldsymbol{f}}_f^C(\boldsymbol{U}/\rho; \mu) \cdot \boldsymbol{e}_1 \right]_f^{n+i} \right\} = \boldsymbol{0} \quad (13a)$$

$\mathcal{L}_{23}$:

$$\sum_{i=1}^{m} \left\{ \alpha_i \boldsymbol{U}_P^{n+i} + \frac{\beta_i \Delta t}{\delta V_P} \sum_{f:\boldsymbol{n}=\boldsymbol{e}_2} \left[\tilde{\boldsymbol{f}}_f^C(\boldsymbol{U}/\rho; \mu) \cdot \boldsymbol{e}_2 \right]_f^{n+i} + \frac{\beta_i \Delta t}{\delta V_P} \sum_{f:\boldsymbol{n}=\boldsymbol{e}_3} \left[\tilde{\boldsymbol{f}}_f^C(\boldsymbol{U}/\rho; \mu) \cdot \boldsymbol{e}_3 \right]_f^{n+i} \right\} = \boldsymbol{0} \quad (13b)$$

$\mathcal{S}$:

$$\sum_{i=1}^{m} \left[\alpha_i \boldsymbol{U}_P^{n+i} - \beta_i \boldsymbol{S}\left(\boldsymbol{U}_P^n, \boldsymbol{U}_P^{n+i}\right) \Delta t \right] = \boldsymbol{0} \quad (13c)$$

Here the convective flux functions $\tilde{\boldsymbol{f}}_f^C$ now also include the appropriate pressure gradient terms and $\boldsymbol{S} = \boldsymbol{S}(\boldsymbol{U})$ is the combined effects of diffusive and local processes. Spatial integrations are performed utilizing a one-dimensional FCT method for $\mathcal{L}_1$ (Ref. 50), a two-dimensional FCT method for $\mathcal{L}_{23}$ (Ref. 51), and three-dimensional central differences for $\mathcal{S}$. Fourth-order FCT algorithms are used, whereas the time integration is implemented using a second-order predictor–corrector scheme.

The gas jets investigated emerge into quiescent background with Mach number $M = 0.6$. The jet and background are composed of air at the same uniform initial temperature and pressure. Table 2 lists the various jet simulations discussed in this section, where Reynolds number is based on D_e, U_0, and estimated upper bounds of the effective numerical viscosity of the FCT algorithm[52] (MILES-EU) or the molecular viscosity μ otherwise. As in the case of forced homogeneous isotropic turbulence, thermal effects are neglected.

Figure 7 compares typical jet visualizations based on the velocity data from run rc40 with the corresponding one (at the same time) for rc36. Flow direction is from bottom to top, and the vorticity levels visualized are in the range between 5 and 70% of peak value. Data have been separately normalized with corresponding peak values. Boundaries of downstream sampling subvolumes are indicated schematically. Because simulations rc40 and rc36 were performed on grids F and C, respectively, with otherwise identical conditions, their comparison provides an assessment on the dependence of the jet dynamics on finite Reynolds number and can also be used to address issues of spatial resolution of the simulations. The jet visualizations in Figs. 7 involve instantaneous volume (ray-tracing) renderings of the vorticity magnitude $|\boldsymbol{\omega}|$. The free square jet development is controlled by the dynamics of interacting vortex rings and braid vortices[21] including the following: deformation of virtually flat (or square) initial vortex rings due to Biot–Savart self-induction; hairpin (or braid) vortices aligned with the corner regions, forming in the initial jet shear layer due to vorticity redistribution and stretching induced by the self-deformation of the vortex rings; and strong interactions between ring and hairpin vortices leading to their breakdown as they become more contorted and incoherent farther downstream, where the flow is characterized by elongated worm vortices resembling those typical of fully developed turbulent flows.[15,16] Figure 7 shows good agreement on the large-scale dynamics of ring and hairpin vortices near the jet exit, hence indicating their somewhat faster breakdown farther downstream for larger Reynolds number.

Table 2 Nominal parameters for the simulation of transitional free square jets

Run	Grid	Total cells	Cells/subvol.	*Re*	Simulation	De/θ
rc40	F	$225 \times 174 \times 174$	$140 \times 140 \times 140$	2.2×10^5	MILES-EU	75
rc36	C	$112 \times 87 \times 87$	$67 \times 67 \times 67$	7.8×10^4	MILES-EU	75
sg01	I	$150 \times 110 \times 110$	$90 \times 90 \times 90$	3.2×10^3	MILES-NS	50
sg02	I	$150 \times 110 \times 110$	$90 \times 90 \times 90$	8.5×10^4	MILES-SMG	50
sg03	I	$150 \times 110 \times 110$	$90 \times 90 \times 90$	8.5×10^4	MILES-EU	50

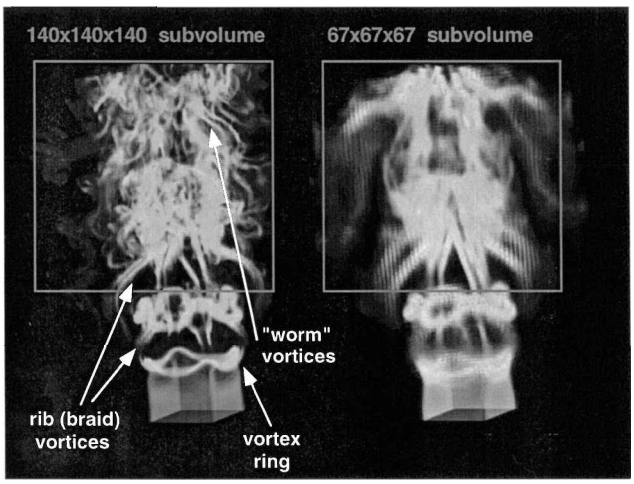

Fig. 7 Instantaneous volume visualization of the vorticity magnitude based on the database of jets rc40 (left) and rc36 (right) at the same time.

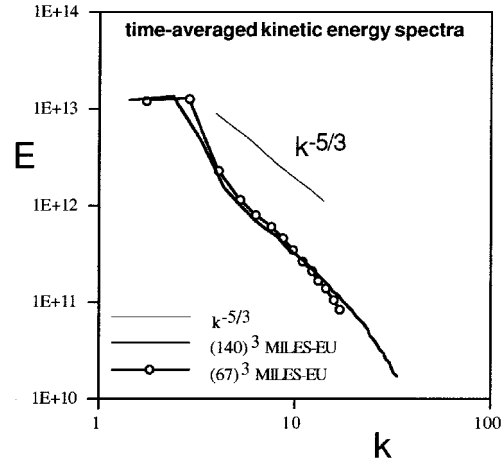

Fig. 8 Time-averaged kinetic energy fluctuation spectra for rc36 and rc40 based on 20 subvolume datasets taken over a time interval of $2/f$.

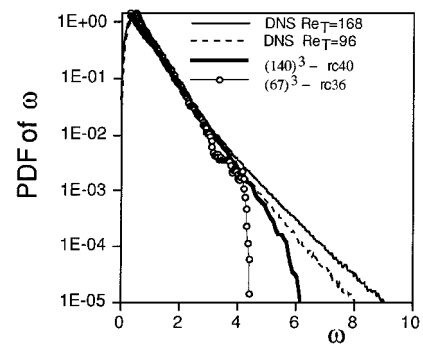

Fig. 9 PDFs of the vorticity magnitude for jets rc36 and rc40 simulated with MILES-EU.

The spectral and PDF analysis that follows focuses on the transition to turbulence in the latter portion of the jets and is used to investigate the small-scale jet behavior captured by the simulations. To minimize the significance of flow transients, we focus the analysis on unsteady flow data for times $t > 3t_0$, where t_0 is the time for streamwise convection with velocity U_0 across the computational domain. We first use spectral analysis to make quantitative statements on the trends of the population of the small scales in the more disorganized downstream portion of the transitional jets. The analysis is based on the velocity databases for the rc36 and rc40 cases with lowest and highest Reynolds number investigated, respectively. Spatial fast Fourier transform (FFT) analysis of the jet databases was performed based on instantaneous velocity data on 140^3 and 67^3 (uniformly spaced) grid subvolumes for rc40 and rc36, respectively. These volumes included only the appropriate downstream portions of the jets chosen symmetrically around the centerline, as indicated in Fig. 7. Time averaging of the velocity and kinetic energy fluctuation spectra is based on data sets for 20 successive times separated by the time step $0.1/f$, where f is the axial forcing frequency introduced earlier. Comparison of the instantaneous velocity spectra[22] indicates an appreciable scatter of the amplitudes for small wave numbers (for example, $|\boldsymbol{k}| < 5$, for rc40) showing the unsteadiness of the contents of the volume analyzed (due to large-scale structures entering and/or leaving the volume) and with the low-wave-number spectral features being specifically dependent on the imposed nozzle geometry and axial forcing frequency. However, the scatter of the amplitudes is fairly small otherwise for the larger wave numbers, for which we thus expect the FFT and PDF analysis that follows to be meaningful.

The largest wave number for which spectral amplitudes are plotted in Fig. 8 corresponds to a wavelength of 4Δ. Figure 8 compares similar time-averaged kinetic energy spectra for rc36 and rc40. As discussed earlier, because these runs were performed on grids F and C with otherwise identical conditions, the comparisons in Fig. 8 reflect on both the spatial resolution of the simulations and the sensitivity of the spectra to changes in Reynolds number. The spectrum shows a small inertial range, characterizing the vortical motions consistent with the $k^{-5/3}$ (inviscid) subrange of the Kolmogorov K41 theory. This inertial range is followed by faster decay of the amplitudes due to the FCT dissipation for wavelengths $\lambda < 10\Delta$. This limiting length scale corresponds to approximately twice the smallest characteristic (full-width) cross-sectional length scales of the elongated vortex tubes in the transitional region of the jet.[22] Figure 8 reaffirms the convergence features suggested by Fig. 7 by showing similar trends and self-similar behaviors for large k.

Figure 9 compares PDFs of $|\omega|$, based on subvolume velocity data for rc36 and rc40, with PDFs based on the higher-Reynolds-number DNS turbulence data[15] ($Re_T = 96$ and 168). As in the preceding section, $|\omega|$ is scaled with its rms value $|\omega|_{\text{rms}}$ for each jet subvolume datum, which defines a characteristic scale. Evaluation of $|\omega|_{\text{rms}}$ is based on velocity data over a time interval $2/f$. A major difference between jet data such as considered here and homogeneous turbulence data relates to the behavior of the PDFs of the vorticity magnitude for small values of $|\omega|$. Because of the transitional and nonhomogeneous nature of the jet regime, e.g., the jet core and surroundings consist mainly of irrotational or nearly irrotational fluid, probabilities of occurrence of small values of, for example, $|\omega| < 0.5$, appear as the largest when based on jet data, in contrast with smaller probabilities there based on analysis of the developed homogenous turbulence data. Otherwise, for the larger values ($|\omega| > 0.5$), PDFs based on both transitional jet flows and homogeneous turbulence show similar monotonically decreasing trends including the range ($1 < |\omega| < 3$) where the slopes of the PDFs appear independent of Reynolds number and tend to coincide. Here we chose to disregard the small $|\omega|$ behavior of the PDFs (closely linked to the specific different natures of jet and box data) and focus on their common features for the larger values of $|\omega|$. For the sake of comparison of the transition to turbulence in the simulated jet flow with the fully developed turbulent regime, the PDFs based on jet subvolume data were renormalized by requiring that they coincide with the PDF of developed turbulence data at a selected intermediate $|\omega|$ ($|\omega| = 2.5$) in the said Reynolds number independent range.

Figure 10 shows CDFs of the vorticity magnitude (for $|\omega| \geq 1$) for rc40 and rc36, superimposed on CDFs based on the DNS data. Figure 10 shows good agreement of rc40 with the DNS data even for fractional volumes of less than 1%, whereas differences between DNS and rc36 are significant much before for fractional volumes between 10 and 1%. Improved agreement with the $Re_T = 96$ DNS data is indicated by Fig. 10. However, it is likely that somewhat smaller $|\omega|_{\text{rms}}$ will be obtained by using longer time-averaging periods, which in turn will have the effect of suggesting larger effective turbulence Reynolds number for MILES-EU on grid F. Because worm vortices typically involve fractional volumes of order 1% or

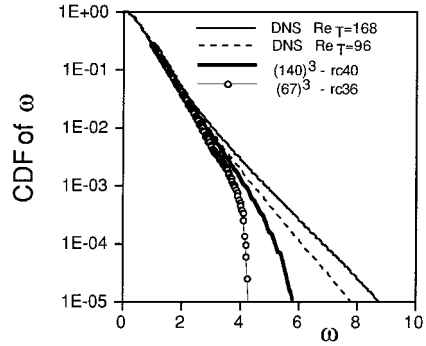

Fig. 10 CDFs of the vorticity magnitude for jets rc36 and rc40 simulated with MILES-EU.

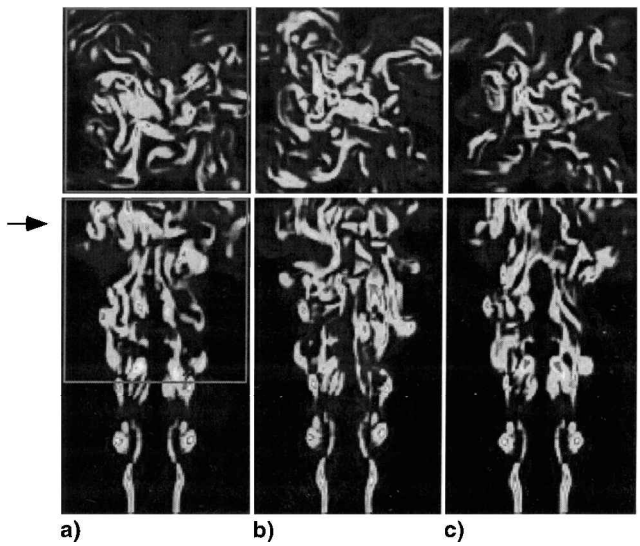

Fig. 11 Instantaneous vorticity distributions at a streamwise plane passing through jet axis (bottom frames) and at a cross-stream plane at indicated streamwise location (top frames). Boundaries of downstream data subvolume are indicated schematically on the left: a) MILES-NS (sg01), b) MILES-SMG (sg02), and c) MILES-EU (sg03).

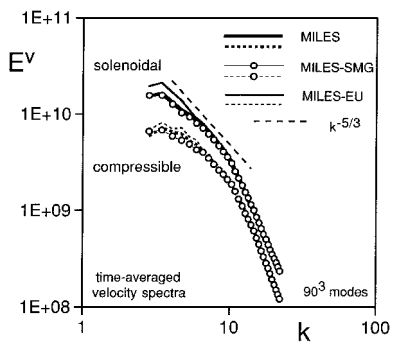

Fig. 12 Time-averaged velocity fluctuation spectra based on downstream subvolume data for the jets of Fig. 11.

less, cf. Ref. 15, only rc40 is, thus, expected to be capable of resolving these vortices, and this is supported by Fig. 7.

Figures 11–13 compare instantaneous vorticity distributions, velocity spectra, and CDFs for MILES (sg01), MILES-SMG (sg02), and MILES-EU (sg03) jet simulations performed on the intermediate resolution I grid with identical initial conditions. The vorticity range is the same for all cases shown in Fig. 11. Here, MILES-SMG involves an effective viscosity including the Smagorinsky viscosity, i.e., $\mu_{\text{eff}} = \mu + \mu_k$ with $\mu_k = c_D \bar{\rho} \Delta^2 \|\boldsymbol{D}\| + \mu^*$, where, as earlier, $c_D = 0.02$ and μ^* is the scalar-valued characteristic viscosity of the FCT scheme and where the strain rates are evaluated based on the raw velocity data. Spectral and CDF analysis was performed using velocity data from the downstream portion of the jets (90^3 subvolume indicated in Fig. 11). The instantaneous velocity fluctuations are decomposed in Fourier space into solenoidal and compressible

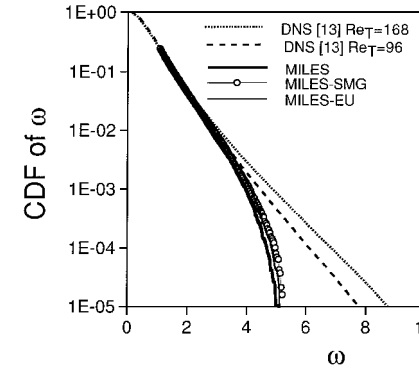

Fig. 13 CDFs of the vorticity magnitude based on downstream subvolume data for the jets of Fig. 11.

components. The bottom frames in Fig. 11 show virtually identical distributions of $|\omega|$ in the lower half of the frames corresponding to the initial larger-scale vortex dynamics, and globally similar but distinctly different local features as we move farther downstream, as the flow regime becomes disorganized and dominated by the presence of elongated vortices. Fig. 12 shows similar velocity spectra for all MILES approaches, indicating the following: 1) somewhat smaller amplitudes for lower wave numbers associated with MILES and MILES-SMG, showing viscous damping of resolved GS features; 2) essentially coincident high-wave-number amplitudes, reflecting the unresolved small-scale viscous effects; and 3) captured inertial subrange and self-similar dissipation regions. The corresponding CDFs of $|\omega|$ compared in Fig. 13 are also very similar and agree well with the CDFs based on DNS homogeneous turbulence data, down to fractional volumes of order 1%, characteristic of the regions filled by worm vortices.

Conclusions

In conventional LES, explicit SGS models are introduced explicitly for closure, but also to provide a mechanism by which dissipation of kinetic energy accumulated at high-wave-numbers may occur. The MILES approach provides a promising alternative involving the solution of the unfiltered NSE with high-resolution monotone algorithms in which the effects of the SGS flow physics on the GS flow are incorporated into the functional reconstruction. With such methods, explicit SGS models can be dispensed with, and the nonlinear high-frequency filters built into the algorithms act as minimal implicit SGS models. Comparison of various conventional LES and MILES models in the studies of forced homogeneous isotropic turbulence showed that the simulated energy spectra depend on the effects of the SGS model only toward the high-wave-number end of the inertial range and into the viscous subrange. LES appears to be independent of the SGS model if the resolution is fine enough to ensure that the cutoff wave number lies in the inertial subrange and if the model can adequately channel kinetic energy out of the wave numbers close to the cutoff wave number to prevent aliasing. All SGS models studied reproduced the DK spectrum reasonably well; in particular, it should be noted that satisfactory results were obtained even at the lowest resolutions considered, irrespective of SGS model. Moreover, integral quantities evaluated based on the energy spectra were well reproduced by all LES models, with somewhat improved predictions from the DSMG and the MILES models. The MILES SGS viscosity is found to be fairly uncorrelated with the coherent structures, although for most conventional LES models, the SGS viscosity is found to peak between closely spaced tubular vortical structures or fat worms, which are regions experiencing intense strain and vortex stretching. Our comparisons indicate that (at least for free shear flows) the MILES approach is generally not worse, and in fact, they suggest that MILES tends to be better once the cutoff wavelength lies within the inertial subrange.

The use of different SGS models in the simulation of developed turbulence results in somewhat different tails of the CDFs of the vorticity magnitude, depending on the specific model and grid resolution. However, the variable tails involve very small fractional

volumes, and all models considered consistently reproduced the basic behavior predicted by DNS: Most of the volume of the resolved flow is occupied by a relatively weak vorticity with intense vorticity regions amounting to only a very small fraction of the volume. The presence of fat worm vortices was clearly captured in the present 64^3 SMG and MILES turbulence simulations; thinner worm vortices were resolved for the intermediate- and finer-resolution jet simulations based on the MILES approach for which CDFs of the vorticity magnitude agreed very well with CDFs based on DNS turbulence data for fractional volumes of up to 1% or less.

Comparison of MILES of transitional freejets initialized with identical laminar conditions, based on the Euler equations (MILES-EU), and the NSE, with (MILES-SMG) or without (MILES) Smagorinsky viscosity, showed very similar results and good agreement with DNS of homogeneous turbulence on their downstream transitional regions, including 1) captured inertial subrange and simulated self-similar dissipation regions within the velocity spectra and 2) almost identical CDFs of the vorticity magnitude. These results reaffirm the virtual independence of SGS model when adequate resolution is involved and in particular support the suitability of the more economical MILES-EU approach for the moderately high-Reynolds-number free shear flow regimes.

The MILES procedure is to be distinguished from UDNS relying on arbitrary methods to emulate the additional required damping, which will not necessarily ensure the correct distribution of energy on the GSs in general. When using MILES, monotonicity and positivity are automatically enforced at length scales of the order of a few grid cells. These features may not be necessary when we focus on the well-resolved, larger flow scales. In this case, using a nonmonotone, implicitly implemented SGS model might also be adequate, e.g., as in Ref. 14, using a third-order upwind biased convection algorithm with a fourth-order dissipation term that channels the GS fluctuations smoothly into the unresolved part of the inertial subrange. Otherwise, if the cutoff lies well within the inertial subrange, monotonicity and positivity are attractive features when steep velocity gradients are involved, if some emulation of the worm vortices characteristic of high-Reynolds-number turbulence at the near-dissipation scale is desired (as well as capturing shocks and/or ensuring that energy, mass density, and species concentrations remain physical, with minimal spurious effects on the well-resolved large-scale flow features). Moreover, in turbulent decay studies in the latter well-resolved simulation regime,[16] MILES/PPM was shown to be capable of emulating the experimentally observed shallower slope (compared to Kolmogorov's K41 slope) of the energy spectra in the near-dissipation region. This can be interpreted as indicating that, in spite of relying on inherently dissipative-type SGS modeling, MILES can implicitly incorporate some degree of desirable backscatter dependent on the existence of the simulated dissipation region, but fairly independent of its precise nature.

We have shown that MILES can be consistently regarded as implicitly implemented LES and have developed a formalism providing mathematical and physical constraints that can be used as guidelines in choosing flux limiters, a choice effectively similar to that of choosing an SGS model in the context of the conventional LES approaches. Because of the nonlinear nature of the flux limiters, however, further study is required to determine ways of constructing practical MILES schemes in this context. Additional requirements on SGS modeling based on topological constraints are also relevant here. The incorrect stress–strain correlation in eddy-viscosity models has been noted, e.g., in Ref. 43, as responsible for the expectation that at best we get good approximations of the turbulent energy dissipation, but not so for the Reynolds stress in the context of this type of model. This drawback can be traced to the inherently different topological features of the strain and Reynolds stress tensors, e.g., Ref. 53, and the particular (isotropic) way in which a relationship is forced upon them through the use of a Smagorinsky-type SGS viscosity. In seeking improved LES, the MILES framework might offer an attractive alternative, due to the inherently tensorial nature of its SGS viscosity.

When turning to more complex flow problems in domains containing walls and requiring nonuniform computational grids, MILES may have some advantage over conventional LES because there is no explicit filtering in MILES and, therefore, no commutation error arises as it would in conventional LES. This may or may not be of practical importance because the commutation error is found to be small in the wall proximity,[24] and it is normally lumped into the a priori unknown SGS stress tensor and flux vector. However, if it is of interest to obtain a mathematically stringent LES formulation, then this problem should be investigated at greater detail. Of more direct consequence is how the SGS stress tensor in both LES and MILES behaves on nonuniform grids and, in particular, how it behaves in the near-wall region. An asymptotic analysis of the flow in the wall proximity shows that $B_{11} = \mathcal{O}(x_2^2)$, $B_{22} = \mathcal{O}(x_2^4)$, $B_{33} = \mathcal{O}(x_2^2)$, and $B_{12} = \mathcal{O}(x_2^3)$, where x_2 is the coordinate in the wall-normal direction. From the definition of the implicit SGS stress tensor, it is clear that these relations do not hold irrespective of the choice of flux limiter. Preliminary MILES of fully developed turbulent channel flows using the described MILES model have been undertaken by the authors and will be the subject of a forthcoming investigation.

Acknowledgments

This research was performed with support from the Office of Naval Research through the Naval Research Laboratory 6.1 Computational Physics task area and the Department of Defense High Performance Computing Modernization Program. The authors thank Javier Jiménez for providing data and helpful information from his direct numerical simulation studies of turbulent flows.

References

[1]Grinstein, F. F., "Open Boundary Conditions in the Simulation of Subsonic Turbulent Shear Flows," *Journal of Computational Physics*, Vol. 115, No. 1, 1994, pp. 43–55.

[2]Galperin, B., and Orszag, S. A., *Large Eddy Simulation of Complex Engineering and Geophysical Flows*, Cambridge Univ. Press, Cambridge, England, UK, 1993, pp. 3–368.

[3]Rogallo, R. S., and Moin, P., "Numerical Simulation of Turbulent Flows," *Annual Review of Fluid Mechanics*, Vol. 16, 1984, pp. 99–137.

[4]Germano, M., Piomelli, U., Moin, P., and Cabot, W., "A Dynamic Sub Grid Scale Eddy-Viscosity Model," *Physics of Fluids A*, Vol. 3, No. 7, 1991, pp. 1760–1765.

[5]Yakhot, V., and Orszag, S., "Renormalization Group (RNG) Methods for Turbulence Closure," *Journal of Scientific Computing*, Vol. 1, No. 1, 1986, pp. 3–51.

[6]Metais, O., and Lesieur, M., "Spectral Large Eddy Simulation of Isotropic and Stably Stratified Turbulence," *Journal of Fluid Mechanics*, Vol. 239, June 1992, pp. 157–194.

[7]Ghosal, S., and Moin, P., "The Basic Equations for the Large Eddy Simulation of Turbulent Flows in Complex Geometry," *Journal of Computational Physics*, Vol. 118, No. 1, 1995, pp. 24–37.

[8]Ghosal, S., "An Analysis of Numerical Errors in Large-Eddy Simulations of Turbulence," *Journal of Computational Physics*, Vol. 125, No. 1, 1996, pp. 187–206.

[9]Fureby, C., "On Sub Grid Scale Modeling in Large Eddy Simulations of Compressible Fluid Flow," *Physics of Fluids*, Vol. 8, No. 5, 1996, pp. 1301–1311.

[10]Vreman, B., Geurts, B., and Kuerten, H., "Realizability Conditions for the Turbulent Stress Tensor in Large Eddy Simulation," *Journal of Fluid Mechanics*, Vol. 278, Nov. 1994, pp. 351–362.

[11]Menon, S., Yeung, P. K., and Kim, W. W., "Effect of Subgrid Models on the Computed Interscale Energy Transfer in Isotropic Turbulence," *Computers and Fluids Journal*, Vol. 25, No. 2, 1996, pp. 165–180.

[12]Fureby, C., Tabor, G., Weller, H. G., and Gosman, A. D., "A Comparative Study of Sub Grid Scale Models in Isotropic Homogeneous Turbulence," *Physics of Fluids*, Vol. 9, No. 5, 1997, pp. 1416–1429.

[13]Boris, J. P., Grinstein, F. F., Oran, E. S., and Kolbe, R. J., "New Insights into Large Eddy Simulation," *Fluid Dynamics Research*, Vol. 10, No. 4–6, 1992, pp. 199–227.

[14]Tsuboi, K., Tamura, T., and Kuwahara, K., "Numerical Study of Vortex Induced Vibration of a Circular Cylinder in High Reynolds Number Flow," AIAA Paper 89-1824, Jan. 1989.

[15]Jiménez, J., Wray, A., Saffman, P., and Rogallo, R., "The Structure of Intense Vorticity in Isotropic Turbulence," *Journal of Fluid Mechanics*, Vol. 255, Oct. 1993, pp. 65–90.

[16]Porter, D. H., Pouquet, A., and Woodward, P. R., "Kolmogorov-Like Spectra in Decaying Three-Dimensional Supersonic Flows," *Physics of Fluids*, Vol. 6, No. 6, 1994, pp. 2133–2142.

[17]Oberman, E. A., and Zabusky, N. J., "Evolution and Merger of Isolated Vortex Structures," *Physics of Fluids*, Vol. 25, No. 8, 1982, pp. 1297–1305.

[18]Steinhoff, J., and Underhill, D., "Modification of the Euler Equations for 'Vorticity Confinement': Application to the Computation of Interacting

Vortex Rings," *Physics of Fluids*, Vol. 6, No. 8, 1994, pp. 2738–2744.

[19]Gathmann, R. J., Si-Ameur, M., and Mathey, F., "Numerical Simulations of Three-Dimensional Natural Transition in the Compressible Confined Shear Layer," *Physics of Fluids*, Vol. 5, No. 11, 1993, pp. 2946–2968.

[20]Grinstein, F. F., Gutmark, E. J., Parr, T., Hanson-Parr, D., and Obeysekare, U., "Streamwise and Spanwise Vortex Interaction in an Axisymmetric Jet. A Computational and Experimental Study," *Physics of Fluids*, Vol. 8, No. 6, 1996, pp. 1515–1524.

[21]Grinstein, F. F., "Self-Induced Vortex Ring Dynamics in Subsonic Rectangular Jets," *Physics of Fluids*, Vol. 7, No. 10, 1995, pp. 2519–2521.

[22]Grinstein, F. F., and DeVore, C. R., "Dynamics of Coherent Structures and Transition to Turbulence in Free Square Jets," *Physics of Fluids*, Vol. 8, No. 5, 1996, pp. 1237–1251.

[23]Möller, S. I., Lundgren, E., and Fureby, C., "Large Eddy Simulation of Unsteady Combustion," *26th Symposium (International) on Combustion*, Combustion Inst., Pittsburgh, PA, 1996, pp. 241–248.

[24]Lions, P. L., *Mathematical Topics in Fluid Mechanics*, Oxford Science, Oxford, England, UK, 1996, pp. 1–16.

[25]Fureby, C., and Tabor, G., "Mathematical and Physical Constraints of Large Eddy Simulations," *Journal of Theoretical and Computational Fluid Dynamics*, Vol. 9, No. 2, 1997, pp. 85–102.

[26]Clark, R. A., Ferziger, J. H., and Reynolds, W. C., "Evaluation of Subgrid Scale Models Using an Accurately Simulated Turbulent Flow," *Journal of Fluid Mechanics*, Vol. 91, Pt. 1, 1979, pp. 1–16.

[27]Speziale, C. G., "Galilean Invariance of Sub Grid Scale Stress Models in the Large Eddy Simulation of Turbulence," *Journal of Fluid Mechanics*, Vol. 156, July 1985, pp. 55–62.

[28]Yoshizawa, A., "Statistical Theory for Compressible Shear Flows, with the Application to Subgrid Modeling," *Physics of Fluids*, Vol. 29, No. 7, 1986, pp. 2152–2163.

[29]Erlebacher, G., Hussaini, M. Y., Speziale, C. G., and Zang, T. A., "Toward the Large-Eddy Simulation of Compressible Turbulent Flows," *Journal of Fluid Mechanics*, Vol. 238, May 1992, pp. 155–185.

[30]Härtel, C., Kleiser, L., Unger, F., and Friedrich, R., "Subgrid-Scale Energy Transfer in the Near Wall Region of Turbulent Flows," *Physics of Fluids*, Vol. 6, No. 9, 1994, pp. 3130–3143.

[31]Fletcher, C. A. J., *Computational Techniques for Fluid Dynamics*, Vol. 1, Springer–Verlag, Berlin, 1988, p. 242.

[32]Godunov, S. K., "A Difference Method for Numerical Calculation of Discontinuous Solutions of the Equations of Hydrodynamics," *Matematicheskii Sbornik*, Vol. 47, No. 3, 1959, pp. 271–306.

[33]Boris, J. P., and Book, D. L., "Flux Corrected Transport I, SHASTA, a Fluid Transport Algorithm that Works," *Journal of Computational Physics*, Vol. 11, No. 1, 1973, pp. 38–69.

[34]LeVeque, R. J., *Numerical Methods for Conservation Laws*, 2nd ed., Birkhäuser Verlag, Berlin, 1992, pp. 173–192.

[35]Harten, A., "High Resolution Schemes for Hyperbolic Conservation Laws," *Journal of Computational Physics*, Vol. 49, No. 3, 1983, pp. 357–393.

[36]Gaskell, P. H., and Lau, A. K. C., "Curvature Compensated Convective Transport: SMART, A New Boundedness Preserving Transport Algorithm," *International Journal for Numerical Methods in Fluids*, Vol. 8, No. 6, 1988, pp. 617–641.

[37]Darwish, M. S., "A New High-Resolution Scheme Based on the Normalized Variable Formulation," *Numerical Heat Transfer*, Vol. 24, No. 3, 1993, pp. 353–371.

[38]Courant, R., Isaacson, E., and Rees, M., "On the Solution of Nonlinear Hyperbolic Differential Equations by Finite Differences," *Communications on Pure and Applied Mathematics*, Vol. 5, No. 3, 1952, pp. 243–255.

[39]van Leer, B., "Towards the Ultimate Conservation Difference Scheme I. Monotonicity and Conservation Combined in a Second-Order Scheme," *Journal of Computational Physics*, Vol. 14, No. 3, 1974, pp. 361–370.

[40]Jasak, H., "Error Analysis and Estimation for the Finite Volume Method with Application to Fluid Flows," Ph.D. Thesis, Dept. of Mechanical Engineering, Imperial College, London, April 1997.

[41]Leonard, A., "Energy Cascade in Large Eddy Simulation of Turbulent Fluid Flows," *Advances in Geophysics*, Vol. 18A, 1974, pp. 237–248.

[42]Bardina, J., Ferziger, J. H., and Reynolds, W. C., "Improved Subgrid Scale Models for Large Eddy Simulations," AIAA Paper 80-1357, July 1980.

[43]Borue, V., and Orszag, S. A., "Local Energy Flux and Subgrid-Scale Statistics in Three Dimensional Turbulence," *Journal of Fluid Mechanics*, Vol. 366, July 1998, pp. 1–31.

[44]Sigga, E. D., and Patterson, G. S., "Intermittency Effects in a Numerical Simulation of Stationary Three Dimensional Turbulence," *Journal of Fluid Mechanics*, Vol. 86, Pt. 3, 1988, pp. 567–592.

[45]Eswaran, V., and Pope, S. B., "An Examination of Forcing in Direct Numerical Simulation of Turbulence," *Computers and Fluids*, Vol. 16, No. 3, 1988, pp. 257–271.

[46]Driscoll, R. J., and Kennedy, L. A., "A Model for the Turbulent Energy Spectrum," *Physics of Fluids*, Vol. 26, No. 5, 1983, pp. 1228–1233.

[47]Briscolini, M., and Santangelo, P., "The Non-Gaussian Statistics of the Velocity Field in Low Resolution Large Eddy Simulations of Homogeneous Turbulence," *Journal of Fluid Mechanics*, Vol. 270, July 1994, pp. 199–217.

[48]Meneveau, C., Lund, T. S., and Cabot, W., "A Lagrangian Dynamic Sub Grid Scale Model of Turbulence," *Journal of Fluid Mechanics*, Vol. 319, July 1996, pp. 353–385.

[49]Vincent, A., and Meneguzzi, M., "The Spatial Structure and Statistical Properties of Homogeneous Turbulence," *Journal of Fluid Mechanics*, Vol. 225, April 1991, pp. 1–20.

[50]Boris, J. P., Gardner, J., Landsberg, A., Patniak, G., and Oran, E. S., "LCPFCT—A Monotone Algorithm for Solving Continuity Equations," U.S. Naval Research Lab., NRL Memorandum Rept. 6410, Washington, DC, April 1993.

[51]DeVore, C. R., "Flux-Corrected Transport Algorithms for Two-Dimensional Compressible Magnetohydrodynamics," U.S. Naval Research Lab., NRL Memorandum Rept. 6544, Washington, DC, Sept. 1989.

[52]Grinstein, F. F., and Guirguis, R. H., "Effective Viscosity in the Simulation of Spatially Evolving Shear Flows with Monotonic FCT Models," *Journal of Computational Physics*, Vol. 101, No. 1, 1992, pp. 165–175.

[53]Hesselink, L., Lavin, Y., Batra, R., and Levy, Y., "The Topology of Symmetric Tensor Fields," AIAA Paper 97-2084, June 1997.

P. Givi
Associate Editor